Remote Sensing of Environment 324 (2025) 114759

Contents lists available at ScienceDirect

Remote Sensing of Environment

journal homepage: www.elsevier.com/locate/rse

Rapid changes in terrestrial carbon dioxide uptake captured in near-real time from a geostationary satellite: The ALIVE framework☆

Danielle Losos [a,b], Sadegh Ranjbar [b], Sophie Hoffman [b], Ryan Abernathey [c,d], Ankur R. Desai [e], Jason Otkin [a], Helin Zhang [f], Youngryel Ryu [f,g], Paul C. Stoy [b,e,*]

[a] Space Science and Engineering Center, University of Wisconsin – Madison, Madison, WI, USA
[b] Department of Biological Systems Engineering, University of Wisconsin – Madison, Madison, WI, USA
[c] Department of Earth and Environmental Sciences, Columbia University, USA
[d] Earthmover, USA
[e] Department of Atmospheric and Oceanic Sciences, University of Wisconsin – Madison, Madison, WI, USA
[f] Research Institute of Agriculture and Life Sciences, Seoul National University, South Korea
[g] Department of Landscape Architecture and Rural Systems Engineering, Seoul National University, South Korea

ARTICLE INFO

Editor: Marie Weiss

Keywords:
Carbon
Gross primary productivity
Geostationary satellite
GOES-R
Machinelearning
Gradient boosting
Downwelling shortwave radiation
Surface reflectance
Eddy covariance
Zarr
Near real-time
Sub-daily
CONUS
Visible
Near infrared
Shortwave infrared
NIRv
NIRvP
MODIS
BESS

ABSTRACT

The terrestrial carbon cycle responds to human activity, ecosystem dynamics, and weather and climate variability including extreme events. Satellite remote sensing has transformed our ability to estimate ecosystem carbon dioxide uptake, the gross primary productivity (GPP), with increasing accuracy and spatial resolution. Many aspects of terrestrial carbon cycling happen quickly on sub-daily or daily scales. These dynamics may not be captured at the temporal scales of typical remote sensing products from polar orbiting satellites – often multiple days or longer. Imagers onboard geostationary satellites measure the Earth system at "hypertemporal" time scales of minutes or less and often have the spectral capabilities to estimate GPP and other surface-atmosphere fluxes using established approaches. Here, we use observations and data products from the Advanced Baseline Imager (ABI) on the Geostationary Environmental Operational Satellite – R Series (GOES-R) to create $ALIVE_{GPP}$ (Advanced Baseline Imager Live Imaging of Vegetated Ecosystems), a GPP product that provides open data on the native five-minute basis of GOES-R CONUS scenes with latency under one day. Our machine learning model, trained on GPP estimates from 111 eddy covariance flux towers with 276 site-years of data spanning tropical to boreal ecosystems, captures up to 70 % of the observed variability when 20 % of tower sites are withheld, with R^2 values of 0.78 (0.82) when aggregating to daily (weekly) periods. We compared $ALIVE_{GPP}$ predictions against eight-day MODIS MOD17A2 GPP estimates and daily GPP estimates from the Breathing Earth System Simulator v2 (BESSv2) and demonstrate how $ALIVE_{GPP}$ simulates the impacts of phenological transitions, flash drought, and hurricanes. Advancements to geostationary satellite imagery, machine learning, and cloud computing make it possible to estimate carbon flux in near real-time and provide new ways to understand the ever-changing carbon cycle and the processes that define it.

1. Introduction

Terrestrial ecosystem gross carbon dioxide uptake, the Gross Primary Productivity (GPP), varies dynamically across time and space in response to drivers that act on time scales from seconds to millennia. Satellite remote sensing has transformed our understanding of GPP and its responses to climate extremes, ongoing climate change, and human activities (Schimel et al., 2015; Xiao et al., 2019). Many of these advancements have come from polar orbiting satellites like MODIS (Heinsch et al., 2006; Running et al., 2004), Landsat (Wulder et al., 2019), Sentinel-2 (Pabon-Moreno et al., 2022), and more, which capture daily to weekly snapshots of the land surface and provide estimates of

☆ This article is part of a Special issue entitled: 'GEO vegetation monitoring' published in Remote Sensing of Environment.

* Corresponding author at: Department of Biological Systems Engineering, University of Wisconsin – Madison, Madison, WI, USA.
E-mail address: pcstoy@wisc.edu (P.C. Stoy).

https://doi.org/10.1016/j.rse.2025.114759
Received 3 July 2024; Received in revised form 1 April 2025; Accepted 11 April 2025
Available online 14 April 2025

GPP on time scales of multiple days to years. In a world where extreme events and rapid ecosystem changes are becoming ever more prevalent and important for carbon cycling (Diffenbaugh et al., 2017; Reichstein et al., 2013; Zscheischler et al., 2014), and where societal decisions are increasingly tied to carbon dynamics (Dilling, 2007; Grace, 2004), rapid inference about terrestrial carbon cycling in near-real time may provide new insights into the processes that control it and ways to manage it (Ryu, 2024).

To observe the carbon cycle as it changes, we need to use all the tools at our disposal. We argue that geostationary satellite observations are an integral approach to this task. Geostationary satellites are neither new nor novel; they have been in continuous use and development since the 1960s (Menzel, 2020; Suomi and Parent, 1968) and are conventionally thought of as "weather satellites" despite their increasing ability to make inferences about the terrestrial surface (Khan et al., 2021) due largely to improvements in their spectral capabilities (Schmit et al., 2017). 'Hypertemporal' (Miura et al., 2019) observations from geostationary satellites on time scales of minutes make it possible to study sub-daily processes to gain a richer understanding of how the land surface responds to environmental variability (Xiao et al., 2021). Frequent observations from geostationary sensors can improve surface data acquisition even on cloudy days by finding cloud-free periods (Jeong et al., 2023). Recent applications of geostationary satellite observations for land surface science include studies of fire (Schmidt, 2020), evapotranspiration (Anderson et al., 2011; Anderson et al., 2007), drought (Otkin et al., 2013), plant phenology (Wheeler and Dietze, 2021; Wheeler and Dietze, 2019), land surface temperature (Desai et al., 2021), methane emissions (Watine-Guiu et al., 2023), sun-induced chlorophyll fluorescence (Jeong et al., 2024), and surface-atmosphere fluxes like ecosystem respiration (Ranjbar et al., 2024a) and GPP (Anderson et al., 2000; A. Khan et al., 2022; Li et al., 2023b; Xiao et al., 2021).

GPP is commonly estimated from satellites using optical vegetation indices that are related to photosynthetically active radiation absorption and therefore photosynthesis (Zeng et al., 2022). Only the latest generation of imagers onboard geostationary satellites measure reflectances in the visible and near infrared that are commonly used to create vegetation indices. These include the Advanced Baseline Imager (ABI) onboard the Geostationary Operational Environmental Satellite - R Series (GOES-R) (Schmit et al., 2017) and similar sensors onboard Himawari 8/9, the GEO-KOMPSAT-2 series, the Fengyun 4 series, and the forthcoming Meteosat Third Generation series of satellites. From this perspective, sub-daily GPP estimation from geostationary satellites is relatively new, and methods to date have largely followed the common 'big leaf' assumption that surface reflectance is related to a bulk leaf area index of plant canopies that responds in aggregate to environmental drivers (Khan et al., 2022; Li et al., 2023b; Ranjbar et al., 2024c; Xiao et al., 2021). There are ongoing efforts to improve remotely-sensed estimates of GPP, such as synthesizing multi-sensor observations and incorporating optimality theory (e.g. Prentice et al., 2024), for which frequent observations can also play an important role. An additional challenge faced by geostationary satellite observations is that they are designed for immediate data dissemination for weather observation and preparedness. The format and volume of data that they transmit in near-real time can be prohibitive (Losos et al., 2024). With advances to machine learning (ML) and cloud computing, we now have additional tools to tackle the challenges posed by geostationary remote sensing for carbon cycle science (Li et al., 2023b).

ML has long been used to study temporal changes to terrestrial carbon dioxide flux measured by eddy covariance (Papale and Valentini, 2003) and to 'upscale' these observations across time and space (Jung et al., 2009) to create global carbon flux data products like FLUXCOM and FLUXCOM-X (Jung et al., 2020; Nelson et al., 2024). Cloud computing improves the efficiency of workflows that can link rapid satellite observations with ML models and disseminate data in accessible formats (Heidinger et al., 2020; Parente et al., 2019; Sun et al., 2019; Yan et al., 2018) to provide near real-time estimates of land surface fluxes.

Here, we develop a combined ML and cloud computing approach using geostationary satellite observations to estimate GPP sub-daily time-steps. Our approach, called 'ALIVE' (Advanced Baseline Imager Live Imaging of Vegetated Ecosystems), trains an ML model on eddy covariance and ABI data to predict GPP ($ALIVE_{GPP}$) at five-minute intervals with a latency under one day. The objective of this study is to assess the performance of $ALIVE_{GPP}$ by comparing it to eddy-covariance data at the the site-level and to the established MODIS GPP algorithm (MOD17A2) (Heinsch et al., 2006; Running and Zhao, 2015) and the Breathing Earth System Simulator v2 (BESSv2) (Li et al., 2023a) across different climatological seasons. We expand this comparison to specific case study events to demonstrate how $ALIVE_{GPP}$ simulates the response of the terrestrial carbon cycle to phenology, flash drought, and hurricanes (Jeong et al., 2023; Khan et al., 2022; Li et al., 2023b; Xiao et al., 2021). Our analysis provides insight into how sub-daily $ALIVE_{GPP}$ estimates can improve understanding of the processes that control carbon flux, while also critiquing its estimates with an eye toward further improvements.

2. Methods

We first describe the eddy covariance and ABI data used to train $ALIVE_{GPP}$. Then we elaborate on the $ALIVE_{GPP}$ model development, performance evaluation and feature selection. All these elements come together in our cloud-native workflow, which showcases how we leverage cloud-native platforms to estimate GPP in near real-time.

2.1. GOES-R and the ABI

The GOES mission began in 1974 (Menzel, 2020) and continues through the latest generation, GOES-R, which includes GOES-16 through GOES-19. The ABI is the primary Earth-observing sensor aboard GOES-R satellites and measures radiation within 16 discrete spectral bands from the visible to thermal infrared, with nominal spatial resolutions between 0.5 and 2 km at nadir. In the operational scan mode (Mode 6), the ABI images the Western Hemisphere 'full disk' at 10-min intervals, the CONUS at 5-min intervals, and two 1000 × 1000 km mesoscale domains at 1-min intervals (or both at 30 s intervals) that can be repositioned to monitor key meteorological events (Schmit et al., 2017; Schmit and Gunshor, 2020).

We collected ABI data products from GOES-16 for August 2019–December 2022 for 314 pixels in which Ameriflux and NEON eddy covariance towers were located. Pixel locations were terrain-corrected to account for the parallax effect which displaces pixels at high elevation due to the large sensor view zenith angle of GOES-16, as described in Losos et al. (2024). The ABI data include top of atmosphere brightness temperatures and reflectances across all 16 bands from the L2 Cloud and Moisture Imagery (CMI) product (Schmit and Gunshor, 2020), bidirectional reflectance factors (BRFs) for bands 1–3, 5, and 6 calculated for the Land Surface Albedo product and estimated under clouds as described in He et al. (2019), downwelling shortwave radiation (DSR) (Laszlo et al., 2020), land surface temperature (LST) (Yu et al., 2008; Yu and Yu, 2020), cloud detections from the Clear Sky Mask (Heidinger et al., 2020), aerosol detection (Kondragunta et al., 2020), and optical depth (Fu et al., 2023; Zhang et al., 2020).

After determining that the hourly ABI DSR and LST products were too infrequent for five-minute GPP estimation, we created our own higher resolution '$ALIVE_{DSR}$' and '$ALIVE_{LST}$' intermediary products to use instead (Ranjbar et al., 2024d; Ranjbar et al., 2024b). Further issues with these products are the coarse 0.25-degree spatial resolution of ABI DSR product (compared to the 2 km native resolution of most ABI data products) and the data gaps under clouds for the clear-sky ABI LST product. $ALIVE_{DSR}$ is produced using a gradient boosting regression (GBR) ML model, trained on surface DSR observations from radiometers

Table 1
Summary of input products and indices used in the GBR model for $ALIVE_{GPP}$ estimation. *$ALIVE_{DSR}$ and $ALIVE_{LST}$ use a subset of CMI observations described in Ranjbar et al. (*2024b, 2024d*).

Product/ Index	Source	Description	Role
BRF 1 (0.47 μm)	ABI Sensor	Bidirectional Reflectance Factor for blue wavelengths	Input for GPP estimation
BRF 2 (0.64 μm)	ABI Sensor	Bidirectional Reflectance Factor for red wavelengths	Input for GPP estimation
BRF 3 (0.86 μm)	ABI Sensor	Bidirectional Reflectance Factor for near-infrared wavelengths	Input for GPP estimation
BRF 5 (1.6 μm)	ABI Sensor	Bidirectional Reflectance Factor for shortwave infrared wavelengths	Input for GPP estimation
BRF 6 (2.2 μm)	ABI Sensor	Bidirectional Reflectance Factor for shortwave infrared	Input for GPP estimation
$ALIVE_{DSR}$	Ranjbar et al. (2024c)	All-sky high-frequency gap-free DSR estimates	Input for GPP estimation
$ALIVE_{LST}$	Ranjbar et al. (2024b)	All-sky high-frequency gap-free LST estimates	Input for GPP estimation
NIRvP	Derived from BRF 2, BRF 3 & PAR	NIR reflectance multiplied by photosynthetically active radiation	Input for GPP estimation
sNIRvP	Derived from BRF 2, BRF 3, BRF 6 & PAR	SWIR-enhanced NIR reflectance multiplied by photosynthetically active radiation	Input for GPP estimation
CMI 1–16	ABI Sensor	Climate Monitoring Instrument products	Input for DSR and LST estimation*
SZA and SAA	Calculated by NOAA algorithm	Solar position (solar zenith angle and solar azimuth angle)	Input for DSR and LST estimation
DOY	Python datetime	Day of Year	Input for LST estimation

at hundreds of eddy covariance sites that underwent Ameriflux quality control checks (Pastorello et al., 2020) as described in Ranjbar et al. (2024d). $ALIVE_{DSR}$ is predicted using ABI CMI bands 1, 2, 4, 6, 12, and 15, the solar zenith angle (SZA), and the solar azimuth angle (SAA). The all-sky $ALIVE_{LST}$ is trained on land surface temperature estimates from upwelling longwave radiation measurements from eddy covariance towers using similar approaches, and using CMI bands 7 and 10–16 with SZA, SAA and day of year with GBR represented an improvement over other inputs and ML models like long short-term memory (LSTM) as described in Ranjbar et al. (2024b).

In the present analysis we trained ML models to estimate GPP using ABI observations from GOES-16, currently in the 'GOES-East' position at 72.5° West. GOES-17 ('GOES-West' at 102.5° West) suffered from a malfunctioning loop heat pipe (McCorkel et al., 2019) and was replaced by GOES-18 in 2022, resulting in time series that were too short to optimize the predictive skill of the ML model (Ranjbar et al., 2024c). GOES-19 is currently in the GOES-East position and is currently scheduled to replace GOES-16 in April 2025. We note that the ABI has similar spectral sensitivity to imagers on other geostationary satellite platforms, including Himawari-8/9 and GEO-Kompsat2A, for which GPP algorithms have also been developed and tested (Jeong et al., 2023; Li et al., 2023b; Xiao et al., 2021).

2.2. Eddy covariance

After compiling the database of GOES-16 ABI data products at eddy covariance tower locations (Losos et al., 2024), we added eddy covariance GPP estimates calculated using the Python program 'hesseflux' (Cuntz, 2020). Hesseflux follows REddyProc (Wutzler et al., 2018), and estimates GPP using both daytime (Lasslop et al., 2010) and nighttime (Reichstein et al., 2005) flux partitioning approaches. It also uses established eddy covariance data quality control routines (Papale et al., 2006; Pastorello et al., 2020) including outlier detection and flagging, and filtering for times of low turbulence by setting a minimum threshold friction velocity (u*). For this project we use the median GPP calculated using the well-established nighttime flux partitioning method. GPP and ecosystem respiration (RECO) may be underestimated when excluding subcanopy CO_2 storage measurements from forest sites when calculating NEE (Fu et al., 2018), so forest sites without subcanopy CO_2 storage measurements were excluded from model training and testing. A list of sites used in model testing and training is provided in the Supplementary Material (Table S1). We use units of μmol m^{-2} s^{-1} when studying half-hourly fluxes to align with the most common units used in the eddy covariance community for GPP, and units of g C m^{-2} d^{-1} for daily and longer sums to align with GPP units more common in remote sensing applications.

2.3. Machine learning development and assessment

The ML model used to create $ALIVE_{GPP}$ resulted from extensive testing described in part in previous studies. From Ranjbar et al. (2024c), we determined that a GBR model outperformed several machine learning techniques – including multi-layer perceptron neural networks, support vector regression, and random forest models – in achieving optimal accuracy relative to prediction time, an essential metric for real-time estimations at a continental scale. We employed a Leave-One-Out Cross-Validation (LOOCV) algorithm; 20 % of the eddy covariance sites were randomly designated as held-out 'test sites,' while the remaining 80 % sites were subsequently merged. LOOCV was chosen to ensure that the model is tested on truly unseen sites, addressing concerns about transferability by simulating its performance on new locations as well as new data at different times. This approach helps prevent overfitting and improves generalization (Lumumba et al., 2024). Additionally, training the model on over 100 eddy covariance sites across the U.S. exposed it to diverse environmental and geographic conditions, enhancing its scalability for regional applications. This dataset, comprising 111 sites and 276 site-years across CONUS, was randomly divided into an 80 % training set and a 20 % test set, allowing us to assess the model's generalization beyond the training sites. To enhance the reliability of our results, we conducted 10 distinct training and testing cycles, each involving different combinations of sites for the held-out subset of test sites. This iterative approach facilitated a thorough evaluation of the model's performance across varying conditions. For evaluation, we averaged the statistics from 10 runs of LOOCV and retained the remainder for uncertainty quantification.

We employed a grid search algorithm to optimize the hyperparameter settings for the GBR. The hyperparameters considered included the number of estimators (100, 200, 400, 600, 800, and 1000), maximum depth (5, 10, 15, 20, and 30), minimum leaf sample size (100, 300, 500, and 700), and learning rates (0.005, 0.01, 0.05, and 0.1). Based on the grid search results, we implemented a GBR model with a maximum depth of 15, 400 estimators, a learning rate of 0.01, and a minimum leaf sample size of 300. The 'scikit-learn' Python library (Pedregosa et al., 2011) was utilized for implementing the grid search, machine learning models, and the LOOCV framework.

As predictors in the GBR model for GPP estimation, we utilized BRF products from the ABI sensor (BRF 1, BRF 2, BRF 3, BRF 5, and BRF 6) as well as $ALIVE_{DSR}$ (all-sky DSR estimates described in Ranjbar et al. (2024c)), and $ALIVE_{LST}$ (all-sky LST estimates described in Ranjbar et al., 2024b)) (Table 1). Additionally, we used two indices to serve as proxies for GPP: Near Infrared Reflectance of Vegetation (Badgley et al., 2019; Badgley et al., 2017) (Badgley et al., 2019, Badgley et al., 2017) multiplied by Photosynthetically Active Radiation (PAR, NIRvP, (Dechant et al., 2022), Eq. (1)); and the Shortwave Infrared-Enhanced, Near-Infrared Reflectance of Vegetation (sNIRv, Eq. (2)) multiplied by PAR (sNIRvP, Ranjbar et al., 2024a):

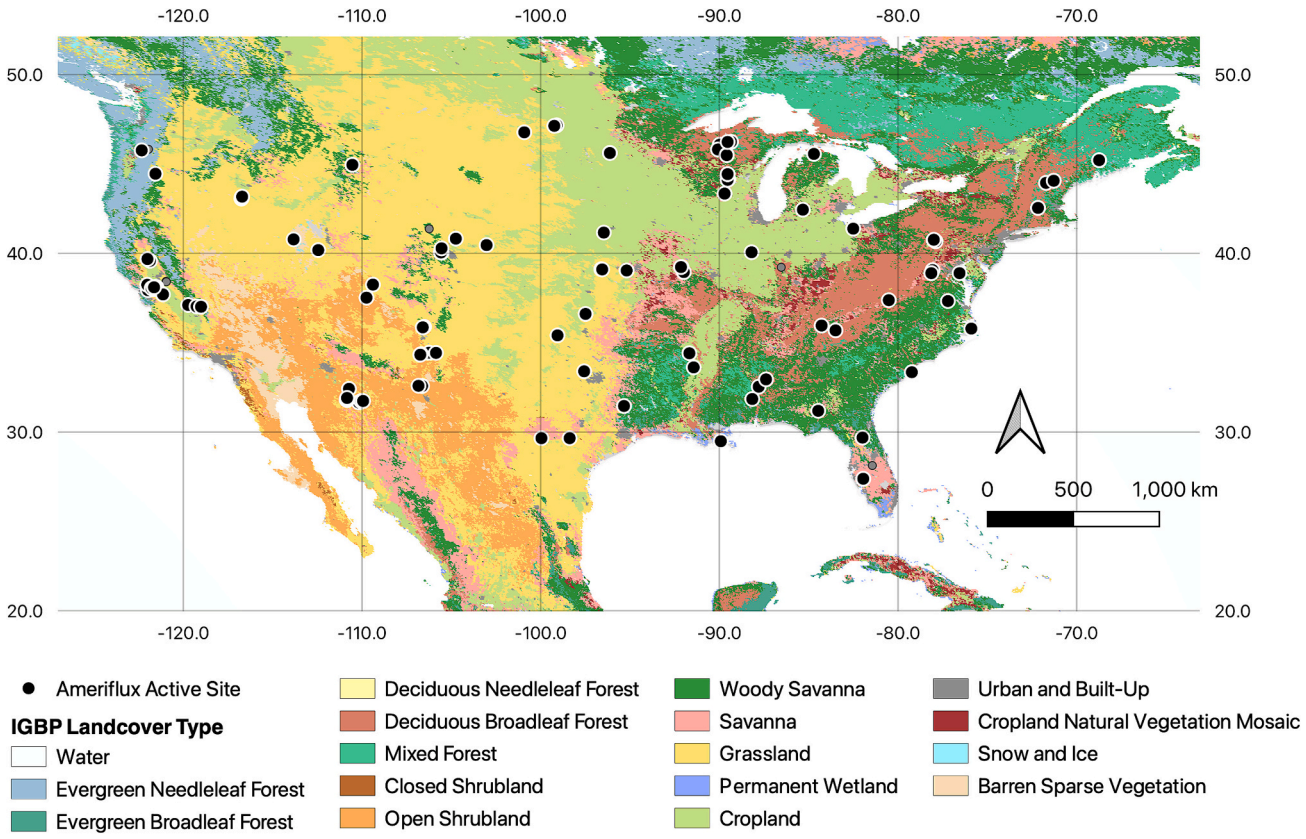

Fig. 1. The Ameriflux eddy covariance tower locations used to train and test $ALIVE_{GPP}$. Sites are mapped over the International Geosphere–Biosphere Programme (IGBP) land cover classes, retrieved from Google Earth Engine.

$$NIRvP = NDVI \times N = \frac{N-R}{N+R} \times N \times PAR \quad (1)$$

$$sNIRv = (NDVI \times LSWI) \times N = \frac{N^2 - N \times S - N \times R + R \times S}{N^2 + N \times S + N \times R + R \times S} \times N \times PAR. \quad (2)$$

In Eq. 2, R, N, and S represent the red (BRF 2 at 0.64 μm), near-infrared (NIR, BRF 3 at 0.86 μm), and shortwave infrared (SWIR, BRF6 at 2.2 μm), respectively.

Following the findings of Khan et al. (2022) and Ranjbar et al. (2024a), we identified NIRvP and sNIRvP as critical inputs for GPP estimation. Ranjbar et al. (2024a) found that incorporating surface shortwave infrared reflectance, particularly from BRF 6 (centered at 2.2 μm), can improve GPP prediction. This enhancement is attributed to the capability of shortwave infrared to reduce interference from soil background, snow cover, and satellite and solar viewing angles (Gu et al., 2021; Lobell et al., 2002; Wang et al., 2017; Xu et al., 2021), which can distort the near-infrared signal in traditional vegetation indices and lead to less accurate GPP estimates. $ALIVE_{DSR}$ is strongly correlated with photosynthetically active radiation, thus it serves as an effective proxy. While we evaluated the inclusion of IGBP vegetation classes, Köppen climate classes, elevation, and day of the year, these factors did not enhance model performance and instead led to overfitting. The relative contribution of each input was calculated using SHapley Additive exPlanations (SHAP, Shapley (1951)) noting that GBR is relatively robust for determining the independent contributions of factors that are correlated by its iterative feature inclusion functionality.

To capture uncertainty, we constructed confidence intervals using a lower bound model at the 5th percentile, an upper bound model at the 95th percentile, and a mean prediction model. The 5th and 95th percentile models, trained with quantile regression, define the bounds of a confidence interval that represents prediction uncertainty (Arkov, 2023; Sluijterman et al., 2024).

2.4. Workflow

Our cloud-native workflow aimed to optimize efficiency and scalability and leverage contemporary tools to handle the bottlenecks common in more conventional workflows (Fig. 2). The only inputs required for our ML models are GOES-R ABI Level 2 products, stored on commercial cloud platforms and made freely available to the public through the NOAA Open Data Dissemination program. We confined our workflow to a single cloud-service provider by pulling the GOES data from Google Cloud Storage S3 buckets and running our computations on Google Cloud virtual machines (VMs).

For every 5-min CONUS scan from GOES-16, we ran our ML algorithm to generate a GPP two-dimensional array ('image'). Generating the $ALIVE_{GPP}$ product depended on first generating the intermediary $ALIVE_{DSR}$ and $ALIVE_{LST}$ products (Ranjbar et al., 2024b, 2024d). For one year (2022) of $ALIVE_{GPP}$, we predicted over 210,000 images, including the intermediate products, at over 70,000 timesteps. Predicting ALIVE estimates at one time step took 2–3 min using a VM with 2 CPU and 8 GB memory. Running each task sequentially on one machine would have taken approximately 146 days of computational time. Instead, we scaled our workflow using Coiled, a service that deploys Dask to parallelize Python code and interface with Google Cloud-based VMs. As a result, we easily scaled to run every day of the year in parallel on 365 VMs, cutting computational time down to just 10 h.

We then utilized Earthmover's Arraylake and the Zarr data model to implement a cloud-native data repository (Abernathey et al., 2021). Traditional raster formats for arrays, like netCDFs and GeoTiffs, treat each array as an image with unique metadata. To analyze a time-series of images, it is often necessary to loop through stacks of images, which can be time consuming and computationally intensive (Losos et al.,

2024). Instead, we stored two-dimensional GPP arrays as slices of a three-dimensional Zarr array (a 'data cube'), with time as the third axis. New GPP arrays were appended to the Zarr array, which grew incrementally in the time dimension. We retained the BRF data quality flags (DQFs) which are provided in a corresponding Zarr array as they incorporate cloud mask and BRF quality information. We stored the resulting $ALIVE_{GPP}$ Zarr library in S3-compatible object storage from Tigris Data. To ease data usability, we deployed the Arraylake service to catalog metadata, which enables efficient reading of pieces of the data cube including both time series and images (Fig. 2).

2.5. MODIS, BESSv2, and case studies

We aggregated $ALIVE_{GPP}$ to compare against daily GPP estimates from the Breathing Earth System Simulator v2 (BESSv2) (Li et al., 2023a) and the eight-day MODIS MOD17A2 GPP product (Heinsch et al., 2006; Turner et al., 2006) during the middle of the climatological seasons (DJF, MAM, JJA, SON) in 2022 to highlight differences that may arise during different times of year. These GPP products were chosen because they were the only ones that provided data as recent as 2022 at time of writing, as far as we were aware. We reprojected and adjusted MODIS GPP and BESSv2 to match the $ALIVE_{GPP}$ scale, projection and units. We then demonstrate $ALIVE_{GPP}$ predictions for rapidly evolving flash drought and hurricane events (and fire/monsoon, wildfire smoke, and synoptic meteorology in the Supplemental Material) to highlight use cases and to challenge its ability to make rapid inference as we aim to improve future versions.

3. Results

3.1. Model assessment

$ALIVE_{GPP}$ achieved an R^2 of 0.70 and an RMSE of 5.19 μmol m^{-2} s^{-1} against half-hourly eddy covariance GPP estimates for the testing set (Figs. 3 and 4). Evaluating the model on a half-hourly basis on the entirely held-out test sites resulted in a mean R^2 of 0.67 to 0.70 and a mean RMSE of 5.22 to 6.17 μmol m^{-2} s^{-1}. At a daily resolution, the average R^2 improves to 0.82 for the testing set and 0.78 for the held-out test sites; at an eight-day resolution, it reaches 0.89 for the testing set and 0.82 for the held-out test sites (Figs. 3 and 4). The model averaged 14.3 μs per sample per loop with a standard deviation of 1.6 μs per sample per loop from 7 runs using Google Colab Pro (random access memory (RAM) up to 32 GB and an A100 graphics processing unit (GPU)).

Model uncertainty quantification for 2022 demonstrates that the range of uncertainty varies with the magnitude of flux (Fig. 5), which has also been shown for EC measurements (Richardson et al., 2006). Individual bands as well as vegetation indices together improve the GBR model fit (Fig. 6). The SHAP analysis indicates that the largest contributions to the ML model are from the sNIRvP and NIRvP indices, as also determined by (Ranjbar et al., 2024a). The two most impactful individual bands are BRF5 (1.6 μm) and BRF1 (0.47 μm, Table 1), which are not components of the vegetation indices (eqs. 1 & 2). $ALIVE_{LST}$ is also a key contributor to the model (Fig. 6), which is a new predictor not included in Ranjbar et al. (2024c).

3.2. Comparisons against MODIS GPP and BESSv2

$ALIVE_{GPP}$ tended to be similar to or lower than MODIS GPP in subtropical and tropical regions toward the south of the GOES-R CONUS scene during all four seasons (Fig. 7). Few observations were available from subtropical and tropical ecosystems for $ALIVE_{GPP}$ model training (Fig. 1), and existing comparisons of the MODIS GPP product against subtropical and tropical ecosystem observations are also relatively sparse (Ferreira et al., 2021; Heinsch et al., 2006; Sjöström et al., 2013). Mean $ALIVE_{GPP}$ was lower than MODIS GPP across much of the eastern U.S. during the spring comparison period (Fig. 7) while the distribution of $ALIVE_{GPP}$ was lower than MODIS GPP during the autumn comparison period (Fig. 8). The mean difference between $ALIVE_{GPP}$ and MODIS GPP during the July 2022 comparison period is only 0.633 g C m^{-2} d^{-1} (Fig. 6) but $ALIVE_{GPP}$ is noticeably greater across California's Central Valley that was in the midst of a multi-year drought (DeFlorio et al., 2024) and across a large swath of the south-central United States that was in the midst of a flash drought that we describe in more detail in Section 3.3 below.

We compared $ALIVE_{GPP}$ with BESSv2 during a single day near the midpoints of the 2022 climatological seasons (Fig. 9). (Note also that $ALIVE_{GPP}$ has intermittent gaps in the imagery due to missing BRF data, which occurs infrequently, albeit in this case for parts of the January and April 2022 study days). Compared to MODIS GPP, the peak of the distributions of $ALIVE_{GPP}$ - BESSv2 GPP is more left-skewed; BESSv2 often calculates higher daily GPP than ALIVE (Fig. 10). Small differences in GPP estimation should be expected due to the explicit representation of the sub-daily impacts of clouds in $ALIVE_{GPP}$ via their role in determining DSR. Notably, during the comparison periods, $ALIVE_{GPP}$ is often lower than BESSv2 in the subtropical and tropical regions where there are fewer eddy covariance sites to train the model. $ALIVE_{GPP}$ is also lower than BESSv2 across the southeastern U.S. on April 14, 2022, indicative of differences in modeling leaf-out phenology. $ALIVE_{GPP}$ was also noticeably lower than BESSv2 GPP on July 15th across regions of the U. S. Northern Plains and Canadian Prairie Provinces that are dominated by agriculture (Stoy et al., 2018) and that have relatively few eddy covariance tower data available for model training (Fig. 1). $ALIVE_{GPP}$ is often greater in the south-central U.S. in July during the early stages of flash drought (Fig. 9) for which MODIS GPP estimates also diverged (Fig. 7). We begin our discussion of $ALIVE_{GPP}$ use cases with a closer investigation of this flash drought event.

3.3. Case study: the summer 2022 south-central U.S. flash drought

The south-central U.S. experienced a compound heat + drought event (Yoon et al., 2024) in summer, 2022 that satisfied the definition of a flash drought (Otkin et al., 2018) (a decrease in root zone soil moisture from above the 40th percentile to below the 20th percentile, with a mean rate of decrease no less than the 5th percentile for each five-day period ('pentad') during the drought development period). The south-central U.S. is prone to rapid onset 'flash' droughts (Christian et al., 2019; Leeper et al., 2022; Otkin et al., 2018) that can have either large (Corak et al., 2024; Zhang and Yuan, 2020) or muted (Parazoo et al., 2024) impacts on carbon cycling depending on antecedent vegetation and hydrologic conditions. Flash droughts have occurred more frequently across multiple global regions (Christian et al., 2021) and are projected to occur more frequently in the future (Christian et al., 2023; Yuan et al., 2023). Land surface models often overestimate drought impacts (Ukkola et al., 2016) and it has been argued that remotely sensed observations often underestimate drought impacts (Stocker et al., 2019), leaving many opportunities to improve drought monitoring and modeling (Sippel et al., 2018).

There are notable differences between $ALIVE_{GPP}$ and other GPP data products in the south-central U.S. in July 2022 during the drought event (Fig. 11). Though the U.S. drought monitor (Svoboda et al., 2002) showed that eastern Oklahoma and western Arkansas were drought-free in late June 2022, rapid drought intensification occurred during July, with most of the region experiencing 3 or 4 categories of degradation over a 4-week period (Fig. 11). This rapid transition caused drought-free areas in late June to be in severe (D2) or extreme (D3) drought only a few weeks later (Fig. 11). Nine eddy covariance towers from the study area were included in $ALIVE_{GPP}$ training (Figs. 1 & 11), which already indicated a decline in GPP across much of Oklahoma, Texas, and Arkansas in early July (Fig. 11) with the notable exception of the Mississippi Delta agricultural region with extensive irrigation (Kebede et al., 2014; Runkle et al., 2017; Yasarer et al., 2020). Compared to BESSv2

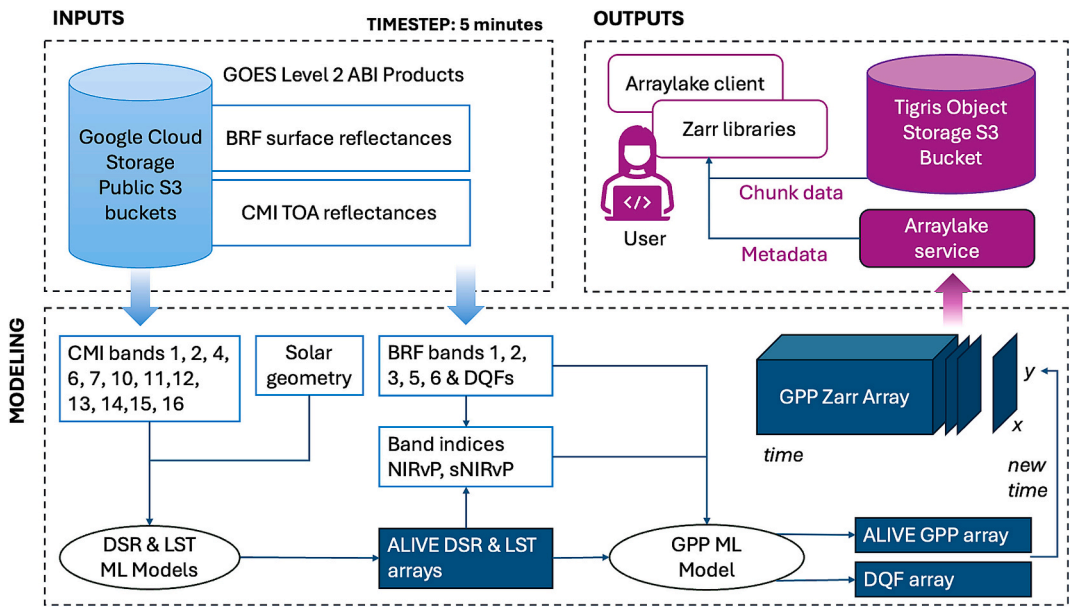

Fig. 2. The cloud-native ALIVE workflow for estimating gross primary productivity (GPP) on a five-minute basis across CONUS using GOES-16 ABI imagery and ML models trained on eddy covariance data.

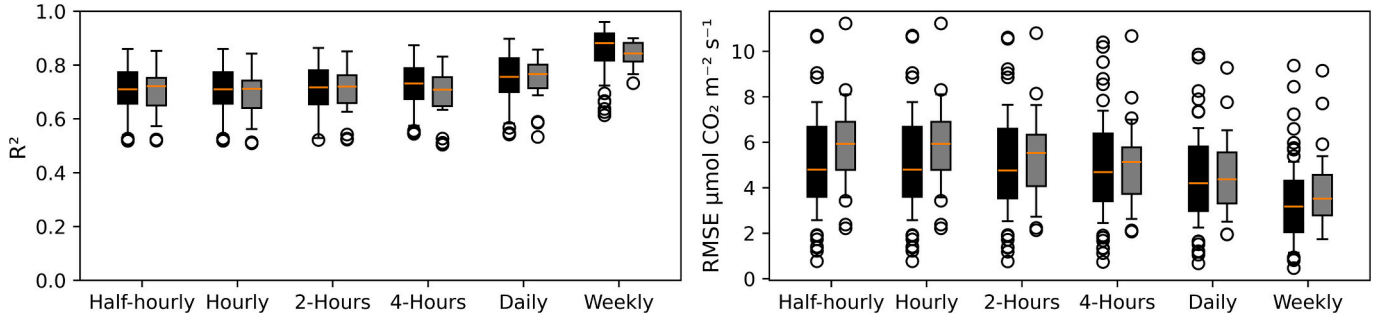

Fig. 3. ALIVE$_{GPP}$ performance for 10 independent model training runs versus tower-based GPP estimates for different temporal resolutions. Results for the testing set are displayed in black and held-out test sites in gray.

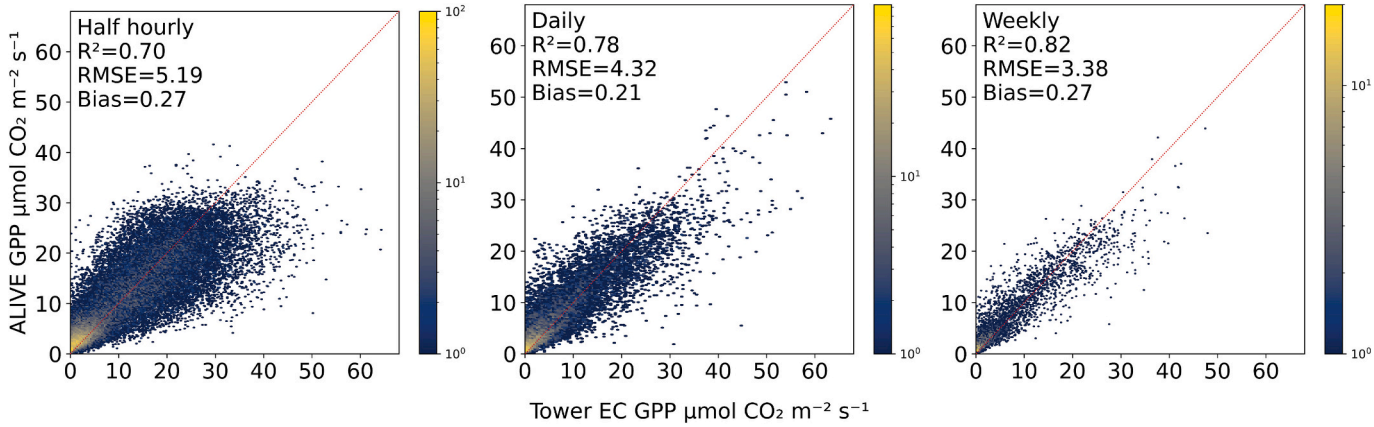

Fig. 4. Heatmaps depicting the correlation between ALIVE$_{GPP}$ and tower-estimated GPP at different temporal resolutions using only data from held-out test sites.

and MODIS GPP products, ALIVE$_{GPP}$ better matched the spatial extent of the class 4 degradation zones denoted by the U.S. drought monitor, especially in southern Oklahoma and northern Texas. The timing of the GPP-depression is similar across products, though the MODIS 8-day product offers less granular temporal detail and smoothes over daily aberrations.

ALIVE$_{GPP}$ predictions at three tower locations within areas impacted by flash drought (with locations noted in Fig. 11) show promising results and also room for improvement (Fig. 12). Western parts of the focal area were already under D0-D2 conditions in late June (note the red box in Fig. 11). ALIVE$_{GPP}$ underestimates tower-estimated GPP before drought onset in the US-xAE western Oklahoma grassland and in the US-RGA

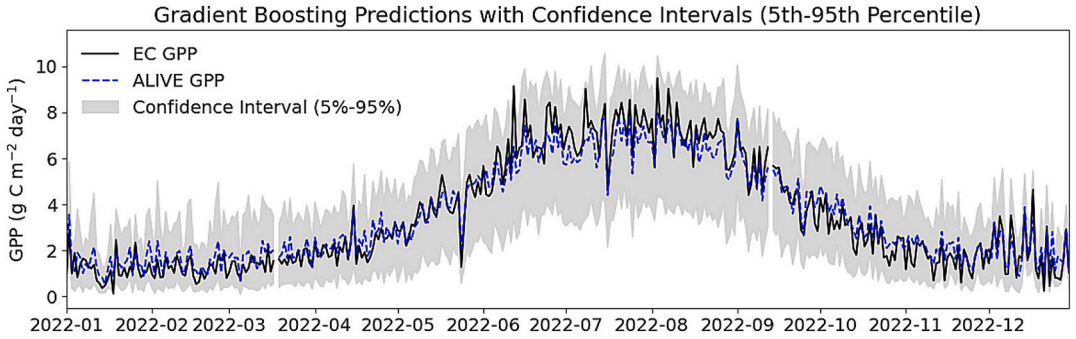

Fig. 5. Daily uncertainty in $ALIVE_{GPP}$, represented by *5 %* and *95 %* confidence intervals, alongside $ALIVE_{GPP}$ and EC tower-estimated GPP measurements for 2022, averaged across all test sites.

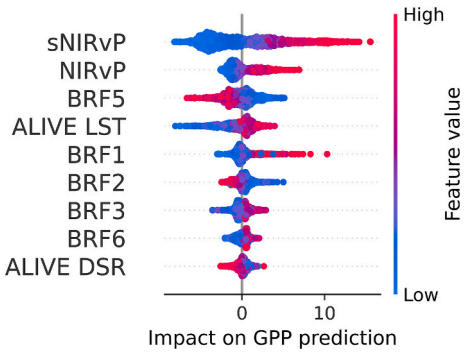

Fig. 6. Shapley Feature Importance Analysis illustrating the contribution of individual features (vegetation indices, individual bidirectional reflectance factors, and data products) to the predictions of $ALIVE_{GPP}$.

maize field in the Mississippi Delta agricultural region in Arkansas and overestimates it in the more mesic US-ARM cropland site in northern Oklahoma (Fig. 12). However, $ALIVE_{GPP}$ successfully simulates the diurnal magnitude and pattern of GPP during the latter stages of the flash drought for all three sites (Fig. 12). Remote sensing often underestimates GPP drought responses (Stocker et al., 2019); $ALIVE_{GPP}$ either overestimates (US-ARM) or underestimates (US-RGA, US-xAE) the magnitude of GPP change before and after the 2022 southern Great Plains Flash Drought.

3.4. Case study: hurricane Ian

Hurricanes can have substantial impacts on ecosystem carbon stocks over long periods of time (Tumber-Dávila et al., 2024) and monitoring their immediate and longer-term impacts is critical for understanding their full carbon cycle consequences (Reed et al., 2025). Hurricane Ian made landfall in southwestern Florida on September 28th, 2022 at around 3:05 EDT (19 UTC) as a Category 5 storm with an estimated maximum wind speed of 125 kt (232 km hr^{-1}) (Bucci et al., 2023) and resulted in 161 casualties with estimated losses exceeding $100 billion

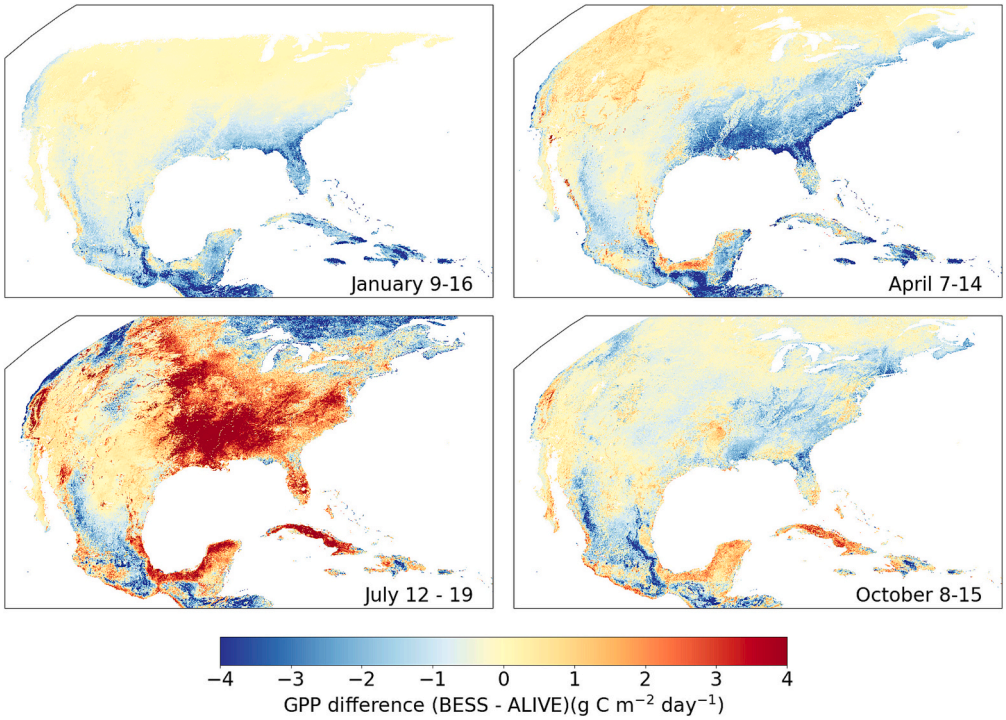

Fig. 7. The difference between the average daily $ALIVE_{GPP}$ and MODIS GPP over eight-day periods that represent the midpoint of climatological seasons in January (upper left), April (upper right), July (lower left) and October (lower right) in 2022. Positive values indicate that $ALIVE_{GPP}$ estimates have greater magnitude.

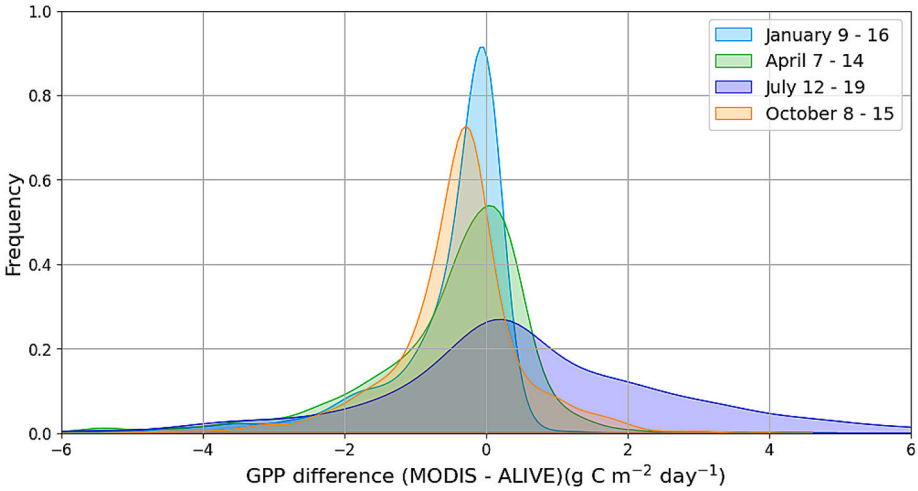

Fig. 8. The frequency distributions of ALIVE$_{GPP}$ - MODIS GPP average daily difference estimates for the eight-day periods at roughly the midpoints of the 2022 climatological seasons as described in Fig. 7.

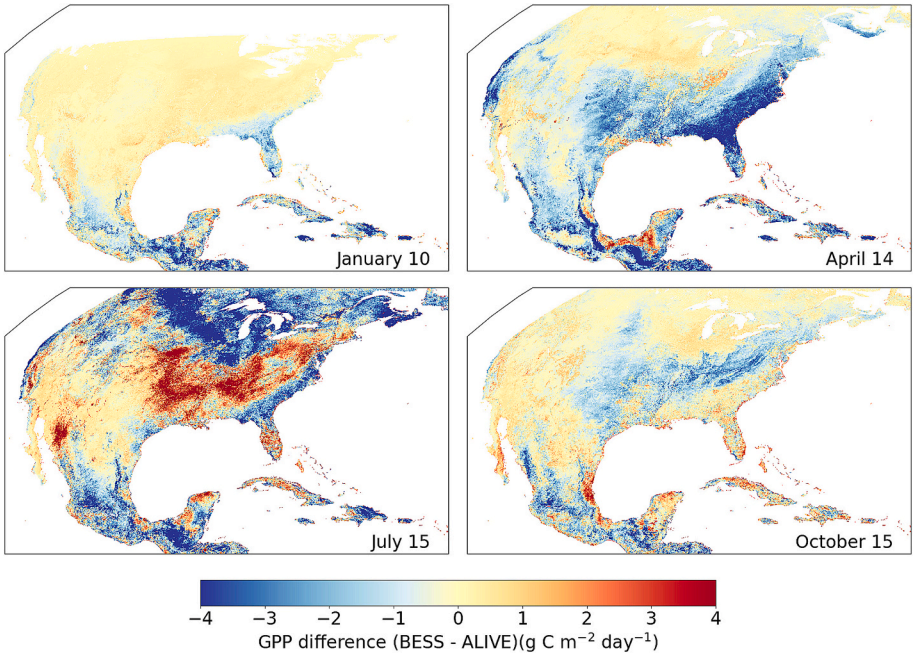

Fig. 9. The difference between daily ALIVE$_{GPP}$ and BESSv2 GPP estimates for the middle of climatological seasons in January (upper left), April (upper right), July (lower left) and October (lower right) in 2022. Positive values indicate that ALIVE$_{GPP}$ estimates have greater magnitude.

(NCEI, 2024). Clouds from Ian decreased ALIVE$_{GPP}$ to values near 0 μmol m^{-2} s^{-1} during much of the event (Fig. 13). We calculated the difference between ALIVE$_{GPP}$ sums from 10 to 14 (Eastern Standard Time) for September 31 and September 23 – the period four days after landfall minus four days before landfall with a focus on a four-hour mid-day window with little cloud presence for fair comparison. We found that GPP decreased near the coast and across many inland areas on the order of −0.1 g C m^{-2} four hours^{-1} or more (Fig. 14), and increased across parts of the Everglades to the south, across much of the Miami metropolitan area, and along a strip between the Fort Myers - Cape Coral metropolitan area and Lake Okeechobee that is dominated by agriculture.

A study of vegetation characteristics, in the Supplementary Material, shortly before and after Hurricane Ian helps explain these patterns. Phenocam observations (Seyednasrollah et al., 2019) near the landfall location at the US-ONA eddy covariance research site (Silveira, 2021) and categorized as a grassland (Fig. 14) indicate relatively little visible vegetation damage (Fig. S5) and no change in the noontime green chromatic coordinate (GCC), indicative of vegetation greenness (Richardson et al., 2018), on the days before and after the event (Fig. S6). The decline in GCC at US-xDS further inland is more pronounced (Fig. 16), but only changed from 0.40 to 0.38. Eddy covariance data was not available from either tower, emphasizing the importance of remote sensing-based estimates to quantify the impacts of extreme events. In brief, the largest immediate declines in ALIVE$_{GPP}$ due to Hurricane Ian were largely limited to regions near landfall and near the coast (Fig. 14) (Turner et al., 2023) with localized areas of lower GPP further inland (Coch, 2020).

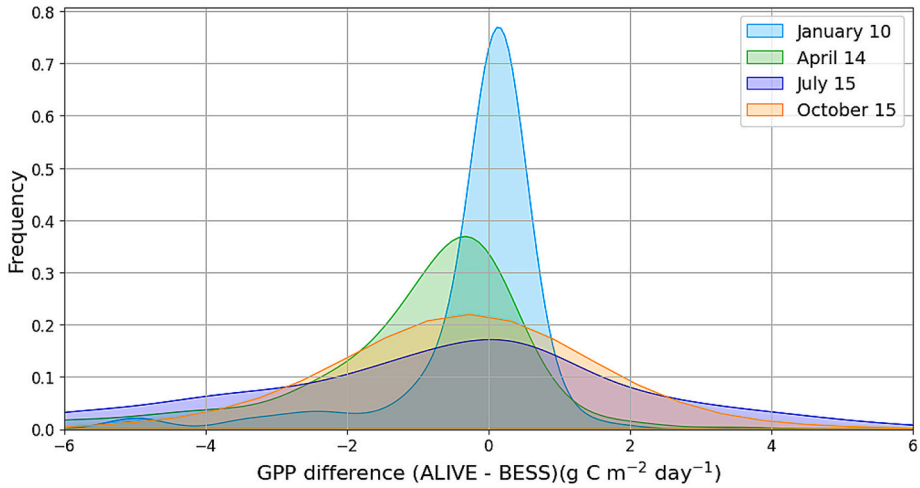

Fig. 10. The frequency distributions of ALIVE$_{GPP}$ - BESSv2 GPP estimates for single days during the four 2022 climatological seasons as described in Fig. 9.

4. Discussion

4.1. Overview

Advances to geostationary satellite imagery, ML, and cloud computing open new avenues for understanding carbon cycle processes (Jeong et al., 2023; A. Khan et al., 2022; Xiao et al., 2021). Careful study of ALIVE$_{GPP}$ predictions against daily (BESSv2) and eight-day (MODIS) GPP data products, and with respect to notable recent extreme climate events (Figs. 9–16), reveals potential benefits but also avenues for improvement. We briefly discuss each with an eye toward further development of geostationary satellite-based estimates of carbon cycling.

4.2. Impacts of rapid ecosystem changes on carbon cycling

From our analyses, ALIVE$_{GPP}$ provides new insights compared to MODIS and BESSv2 regarding the seasonality of GPP across CONUS during spring and autumn. ALIVE$_{GPP}$ helps capture the nuances in the timing of regional phenology changes that geostationary satellites are adept at tracking (Wheeler and Dietze, 2021; Wheeler and Dietze, 2019). One explanation for different seasonal responses is that MODIS GPP uses a constant maximum light use efficiency parameter as a function of ecosystem type whereas photosynthetic capacity (often taken to be the maximum carboxylation rate of Rubisco, $V_{c,max}$) varies with leaf age, resulting in higher values in spring than autumn (Grassi et al., 2005; Way et al., 2017; Wilson et al., 2000). ALIVE$_{GPP}$ stimulates the spatial extent of the July 2022 flash drought with greater similarity to the U.S. Drought Monitor than the other GPP data products (Fig. 11) and mimics the diurnal GPP behavior recorded by eddy covariance towers during later stages of drought (Fig. 12). The ALIVE$_{GPP}$ response to Hurricane Ian is consistent with literature on the magnitude, direction, and time scales of vegetation response to tropical cyclone disturbance (Figs. 13–14), while local increases in GPP point to directions for future study; vegetation function in areas without pronounced hurricane damage may benefit from additional precipitation (Lowman and Barros, 2016; Wang and D'Sa, 2009). From the additional analyses in the Supplemental Material, responses to fire and monsoon transitions follow expectations (Fig. S1), and wildfire smoke and the synoptic patterns that entrained it into the western Great Lakes region caused ALIVE$_{GPP}$ responses that were dynamic and complex (Fig. S2). In this case, multiple interacting processes had complex effects on GPP which points to the need to integrate more observational datasets and perhaps explainable artificial intelligence methods into future iterations of ALIVE$_{GPP}$ to better understand which factors are contributing most strongly to changes in GPP.

4.3. Limitations: GOES-R observations

We used operational NOAA Level 2 ABI products for efficient workflows. Therefore, ALIVE$_{GPP}$ is constrained in time and space by ABI product availability. The primary ALIVE$_{GPP}$ input, BRF, has been operational since August 2021, preventing our extension of the ALIVE$_{GPP}$ historical archive to earlier dates. Surface reflectances are only valid during hours of direct sunlight, and the BRF product designates 67 degrees as a sufficient SZA to generate a valid product. ALIVE$_{GPP}$ matches this limitation by only providing GPP for times and locations where the local SZA is less than 67 degrees, which results in GPP underestimation during early morning and early evening periods. The forthcoming Nadir BRDF-Adjusted Reflectance (NBAR) GOES product may be beneficial for future releases of ALIVE$_{GPP}$, which will normalize for the effects of diurnally varying SZA and ease comparisons against other satellite observations. The routine by which the operational BRF algorithm estimates values under clouds (He et al., 2019) helps ALIVE$_{GPP}$ minimize gaps due to missing data, although gaps remain where there are GOES product outages (note for example small regions of missing data near the Great Lakes in the January comparison with BESSv2 in Fig. 9).

The "ABI Fixed Grid" geostationary projection is not currently terrain-corrected because most ABI products observe the atmosphere rather than the Earth's surface. Pixels at high elevation are displaced from their targets by up to several kilometers due to the large VZA of CONUS by the GOES-16 sensor; the 'parallax effect'. To ensure accuracy when training our model, we geographically aligned Ameriflux towers with uncorrected ABI pixels using a point-based DEM correction method, described in Losos et al. (2024). We recommend users follow this method to adjust location coordinates to match the correct ABI pixel when extracting time-series data. GOES-R image-wide terrain correction is under development and will be applied to future iterations of ALIVE$_{GPP}$.

ALIVE$_{GPP}$ is also limited by spatial resolution. At nadir, the ABI band resolutions are 500 m for red (CMI_02), 1 km for blue (CMI_01) and two near-infrared bands (CMI_03 and CMI_05), and 2 km for all other bands. All multi-band ABI products are created at 2 km resolution with pixel shape becoming more elongated moving away from the nadir point (Losos et al., 2024). The forthcoming Geostationary Extended Observations (GeoXO) mission is scheduled to replace GOES-R starting in 2032. Enhanced spatial resolution will improve to 250 m in the red, 500 m to 1 km across most of the visible, near-infrared, and some infrared bands, which will reduce the impacts of sub-pixel variability, and new bands will detect low-level water vapor (Lindsey et al., 2024; Schmit et al., 2022). In other words, geostationary satellite capabilities will continue to improve, as can their benefit to carbon cycle science with

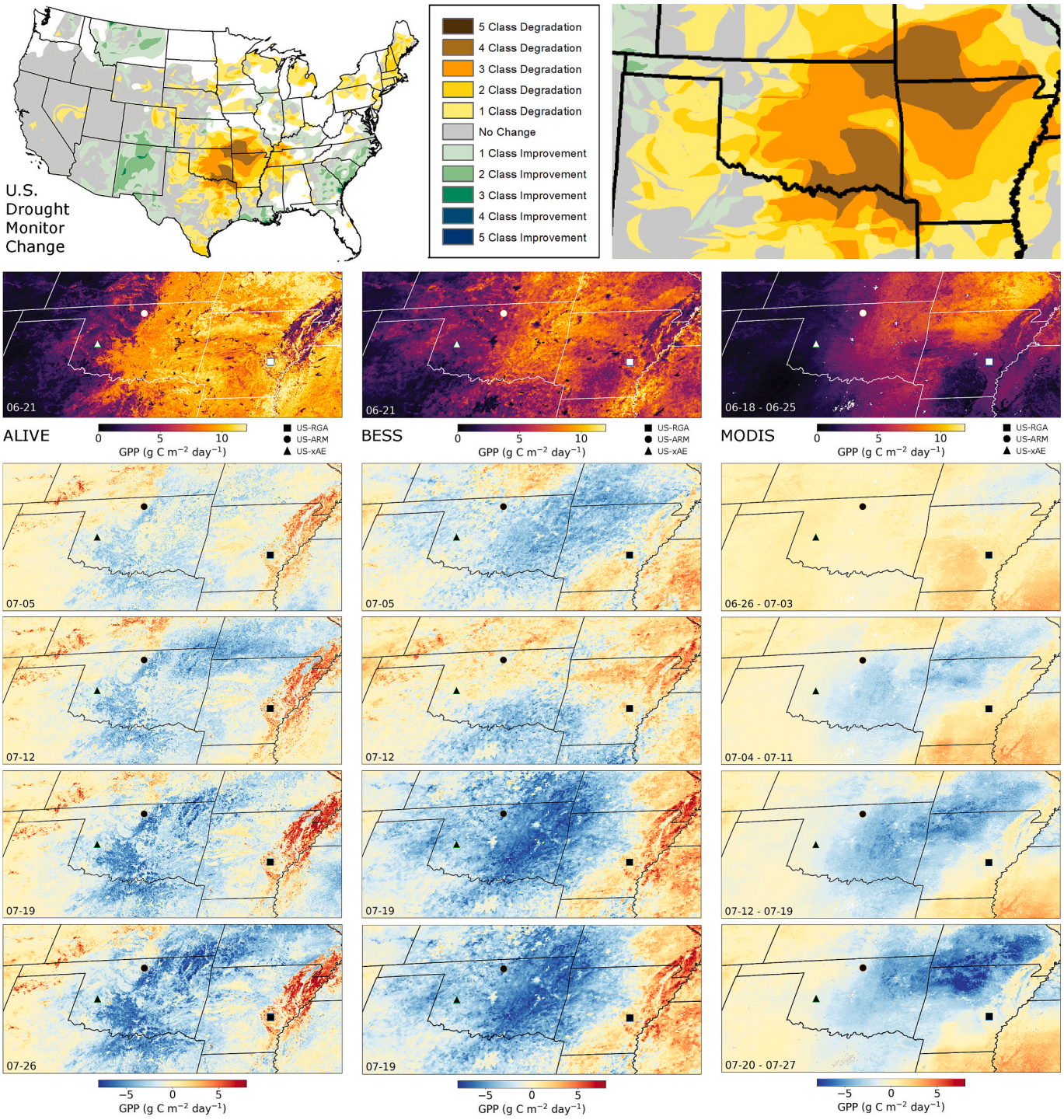

Fig. 11. A comparison of daily $ALIVE_{GPP}$, BESSv2 GPP, and 8-day MODIS GPP estimates from June to July 2022. The top row shows the U.S. Drought Monitor Change Map from Leeper et al. (2022) between June 21 to July 26, with a cut out of the south-central U.S. The columns show ALIVE (left), BESS (center) and MODIS (right) GPP at/around the baseline date of June 21, and difference images showing the change in GPP on subsequent weeks in July. The MODIS images are daily averages across the 8-day periods. Three EC tower sites are mapped as a square (US-RGA), circle (US-ARM) and triangle (US-xAE).

continued algorithm development.

4.4. Limitations: additional data inputs

We estimated GPP using GOES-16 data products alone for the purpose of understanding how well the $ALIVE_{GPP}$ algorithm can work in the absence of other meteorological, atmospheric, or remotely sensed data. We intend to add more observations into the ALIVE workflow (Fig. 2) to help estimate terrestrial carbon and water fluxes, but few if any data products exist at its spatial and temporal resolution and latency. We briefly discuss opportunities for adding additional inputs to improve the skill of $ALIVE_{GPP}$.

At the moment $ALIVE_{GPP}$ only learns about the sub-daily patterns of GPP through its training against eddy covariance estimates of GPP using GOES-R BRF data products, $ALIVE_{DSR}$, $ALIVE_{LST}$, SZA, and SAA. Training the ML model with meteorological data may help $ALIVE_{GPP}$ simulate their impacts on carbon dioxide flux. Even though meteorological data do not always improve ML-based remote sensing predictions of GPP

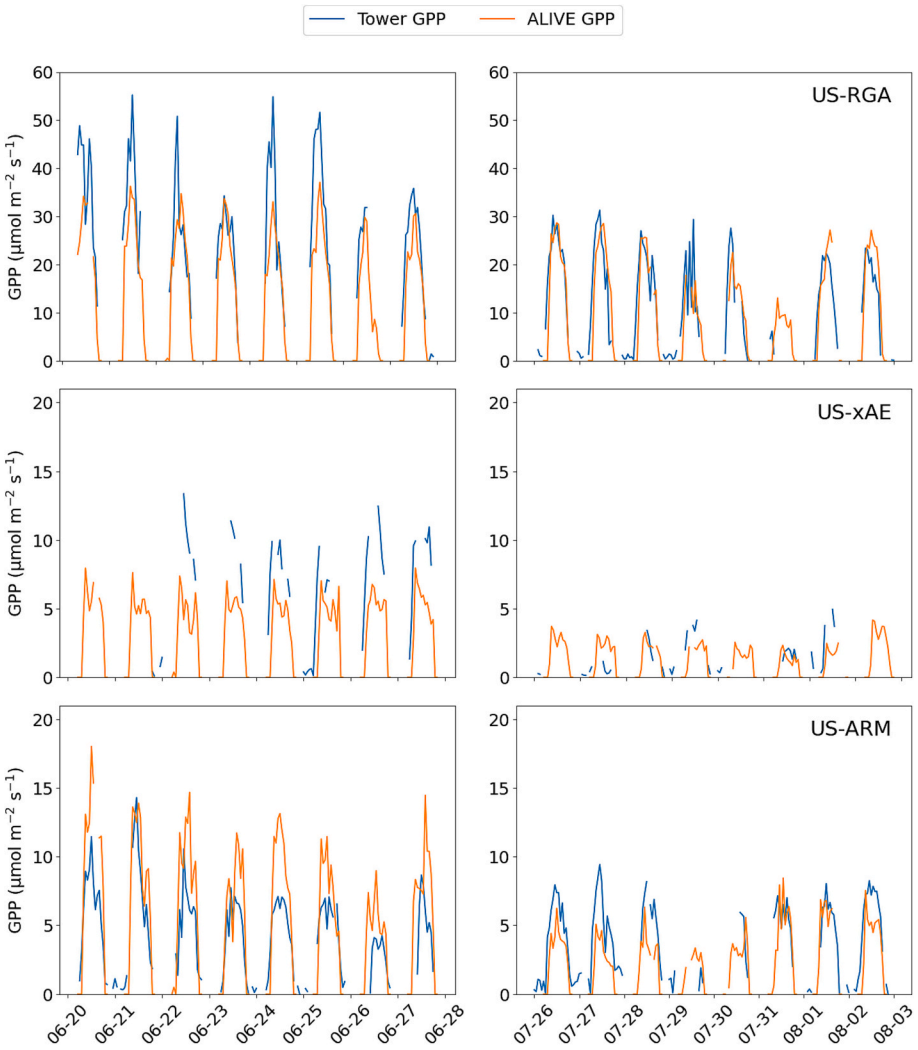

Fig. 12. The diurnal course of $ALIVE_{GPP}$ and GPP derived from eddy covariance towers US-RGA, US-xAE, and US-ARM for eight-day periods before (left column) and during the end stages (right column) of the flash drought in the south-central U.S. during summer 2022 (pictured in Fig. 11).

(Tramontana et al., 2015), it stands to reason that incorporating meteorological data will help infer the impacts of extreme events and sub-daily processes (Jeong et al., 2023; A. Khan et al., 2022; Li et al., 2023b; Xiao et al., 2021) and perhaps help reconcile the tendency of remote sensing products to underestimate GPP impacts (Stocker et al., 2019). As one example, incorporating diffuse DSR into our ML model training did not improve aggregate fit across all sites (data not shown), but it may have been helpful to better disentangle the impacts of wildfire smoke (Fig. S3 & S4). VPD cannot be observed from space but is a critical constraint on GPP (Fu et al., 2022; Novick et al., 2016).

No meteorological datasets available across CONUS to our knowledge have spatial and temporal resolution commensurate with ABI observations. The High-Resolution Rapid Refresh (HRRR) model assimilates multiple meteorological data sources to estimate various meteorological variables at 3 km resolution every hour (Dowell et al., 2022; James et al., 2022). $ALIVE_{GPP}$ could be downscaled to match its resolution, especially if hourly rather than five-minute imagery proves sufficient for capturing sub-diurnal trends in GPP. The HRRR will be replaced by the Rapid Refresh Forecasting System (RRFS) (Alexander et al., 2023; Grim et al., 2024) which will remain on a 3 km grid over North America with further improvements in prediction.

Near-real time estimates of atmospheric stressors like $[O_3]$ are currently unavailable on continental scales but boundary-layer (0–2 km) hourly estimates of key components of tropospheric O_3 chemistry are available as of May 2024 with the launch of TEMPO (Tropospheric Emissions: Monitoring of Pollution) (Naeger et al., 2021; Zoogman et al., 2017). This new geostationary mission measures nitrogen dioxide, sulfur dioxide, other atmospheric pollutants, and UVB radiation and operates on a similar spatial scale as GOES-16 (at 2.1 × 4.5 km^2 at 36.5° N and 100° W near the center of the 'field of regard' across North America). Hourly estimates of boundary-layer $[O_3]$ are available at 8 km resolution to account for signal-to-noise. To the extent that boundary-layer $[O_3]$ provides a reasonable estimate of surface conditions, integrating TEMPO into $ALIVE_{GPP}$ could represent an unprecedented opportunity to understand how the complex spatial and temporal patterns of air pollution impact ecosystem carbon uptake as it occurs (Figs. S3 & S4).

4.5. *Limitations: Eddy covariance*

$ALIVE_{GPP}$ training is also subject to uncertainties in flux partitioning that are inherent to any eddy covariance analyses of carbon cycle processes (Reichstein et al., 2012; Stoy et al., 2006). Ameriflux sites within the GOES-16 CONUS field of view (−81.33 S, 81.33 N, 6.3 E, −156.3 W) were used to train $ALIVE_{GPP}$ (Fig. 1). The only excluded sites with available data at the time of model development were two in Chile. This created a strong bias toward temperate and continental climates and biomes (Fig. 1) and Northern Hemisphere sites. Like all other satellite

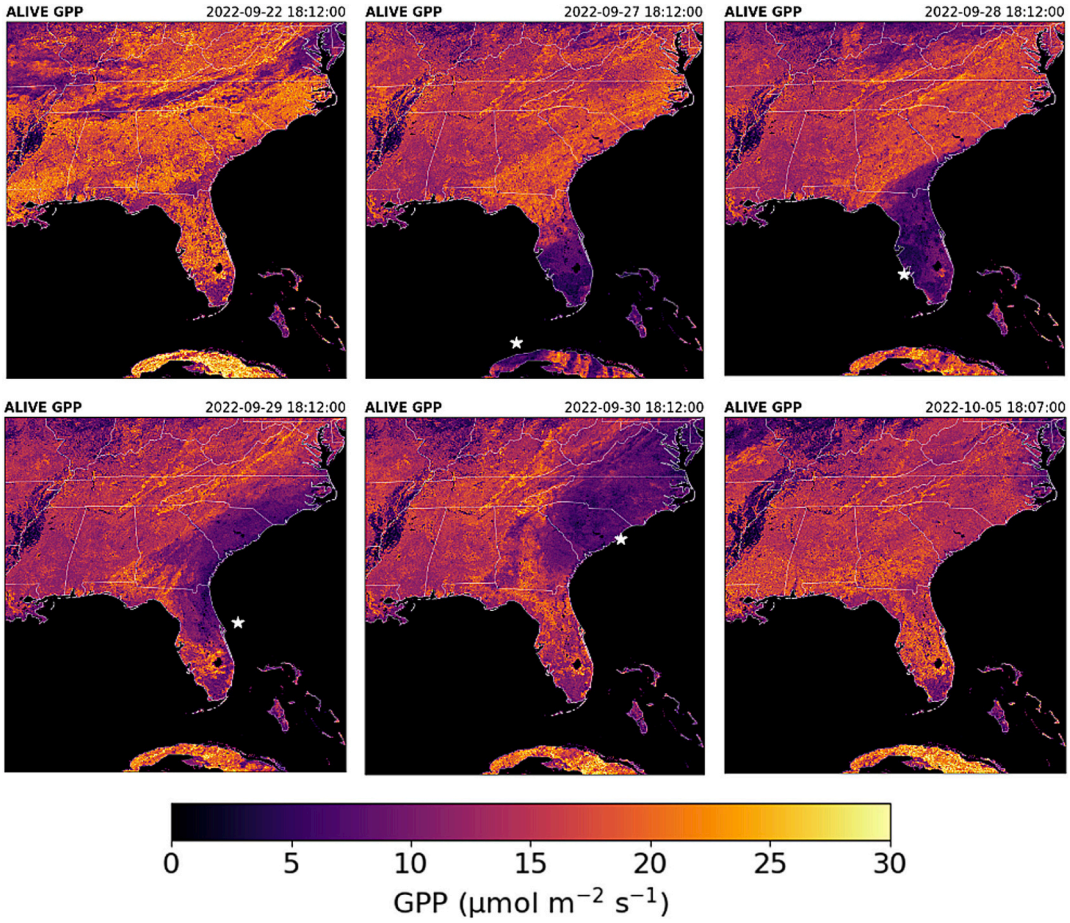

Fig. 13. ALIVE$_{GPP}$ estimates (in μmol m^{-2} s^{-1}) within Hurricane Ian's path through Florida and subsequently South Carolina from September 27th through September 30th, 2022 with comparison images from September 22nd and October 5th, five days before and after the impact of the hurricane. The white star represents the location of the eye of the hurricane (Bucci et al., *2023*).

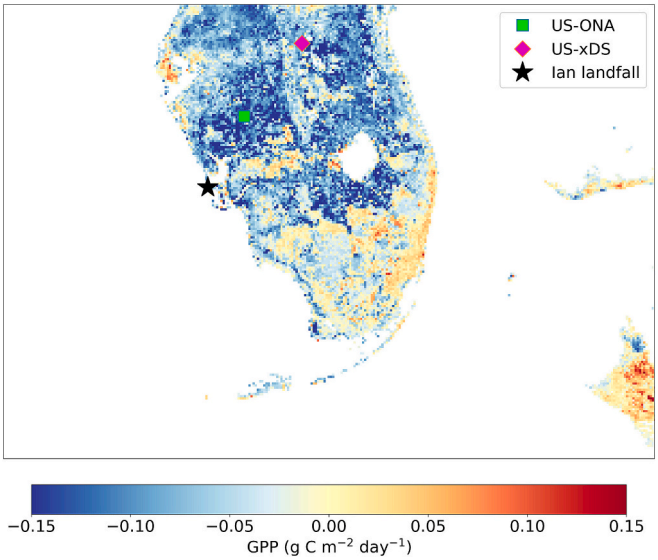

Fig. 14. Difference in ALIVE$_{GPP}$ for four-hour midday sums (between 10:00 and 14:00 EST) between September 23 and September 31, 2022, four days before and after Hurricane Ian's landfall on September 27. Blue values indicate a decrease in GPP between the two time periods. Eddy covariance research tower sites US-ONA and US-xDS and Hurricane Ian's landfall are marked with symbols. *(For interpretation of the references to colour in this figure legend, the reader is referred to the web version of this article.)*

remote sensing studies, we are limited by the representativeness of the dynamic eddy covariance flux footprint within a given ABI pixel or sometimes multiple pixels (Chu et al., 2021). The scale-mismatch is exacerbated by the spatially extensive ABI pixels. This can be a particular problem when assuming a plant functional type within a pixel (Hartley et al., 2017) and adding plant functional type and climate classification resulted in overtraining ALIVE$_{GPP}$. From this perspective it is unclear if ALIVE$_{GPP}$ may be improved by further integrating plant traits (Pavlick et al., 2013), and it would be necessary to have trait maps on fine spatial and temporal resolutions matching GOES scenes and ideally update them in situations of rapid vegetation change. At a minimum, the BESSv2 comparisons suggest large discrepancies during the vegetative growing season across agricultural regions dominated by corn/soy rotations with poor eddy covariance data coverage (Fig. 11), and also subtropical and tropical regions (Fig. 9), which may point to the importance of integrating C3 and C4 plant photosynthetic pathways (Jiang et al., 2021; Li et al., 2023a). ALIVE$_{GPP}$ as written is unable to simulate instantaneous uptake of CO_2 by CAM-dominated ecosystems at night.

We are also constrained by the latency of eddy covariance data. These are often submitted to Ameriflux months to years after collection, which limited our analysis from the 314 sites described in Losos et al. (2024) to the 111 that had any available data during the August 2021–December 2023 period that we used for model testing and training (Table S1). More sites in under-represented regions would improve model fit (Ranjbar et al., 2024c). An emphasis on improved latency across carbon cycle observations and modeling systems would help provide actionable information for carbon cycle decision-making.

4.6. Opportunities: quasi-global geostationary synthesis and remote sensing data fusion

There are ongoing opportunities to benefit from the GeoNEX initiative to integrate and harmonize observations from multiple geostationary platforms worldwide (Nemani et al., 2020; Wang et al., 2020) and expand the spatial reach of $ALIVE_{GPP}$ and similar data products (Li et al., 2023c; Wang and Li, 2022). GeoNEX products currently include variables critical for GPP estimation, including DSR. Global collaboration on estimating surface fluxes from geostationary satellites worldwide, and fusion with satellite observations with finer spatial and spectral resolution (Li et al., 2020; Wu et al., 2015), could help provide carbon flux estimates with high accuracy and low latency that align with decision making and carbon management.

Rapid observations from geostationary satellites may be most useful as a 'hypertemporal' end member of a multi-sensor data fusion approach for quantifying land surface processes (Ghassemian, 2016; Simone et al., 2002). Though spatially coarse, geostationary observations help provide estimates of land surface function and carbon cycling 'everywhere, all of the time' (Baldocchi, 2014). Multiple approaches have already combined inference from polar-orbiting and geostationary satellites to estimate LST at higher spatial and temporal resolutions than individual satellites alone (Li et al., 2020; Wu et al., 2015). Others have gone a step further to integrate multiple remote sensing observations to further develop hyperspatial and hypertemporal estimates of LST (Desai et al., 2021). Looking forward, with improved opportunities to constrain global biomass via forthcoming and ongoing missions like GEDI and ESA-Biomass, additional information on photosynthetic processes from ESA-FLEX and more, and atmospheric carbon dioxide concentration observations from OCO-3, we can further improve our knowledge of carbon cycle processes.

5. Conclusions

$ALIVE_{GPP}$ uses ML and cloud computing to estimate GPP across the GOES-16 CONUS scene on five-minute intervals with latency under one day and stored in public Zarr libraries (Fig. 2). We overcame the processing challenge for geostationary observations where multiple individual files are not designed for time series analysis (Losos et al., 2024). Zarr libraries, which chunk data cubes into smaller pieces, help store these data efficiently and make them more accessible to end-users. Results demonstrate differences in seasonality and sensitivity to extreme events compared with MODIS GPP when aggregated to an 8-day basis (Figs. 7 & 9) and BESSv2 on a daily basis, with notable differences when comparing flash droughts and in regions with relatively little eddy covariance data for training (Figs. 8 & 10). $ALIVE_{GPP}$ demonstrates a rapid response to the 2022 south-central U.S. flash drought with declines in GPP of greater than 5 g C m^{-2} day^{-1} in some areas compared to pre-drought conditions within weeks of drought onset (Figs. 11 & 12). Patterns of GPP recovery after drought and wildfire are captured by $ALIVE_{GPP}$ during brief gaps in cloud cover during the 2022 New Mexico monsoon season (Fig. S2). $ALIVE_{GPP}$ also estimated the dynamic response of GPP to Hurricane Ian in Florida with complex spatial patterns that are consistent with phenocam observations and previous studies of hurricane impacts on vegetation (Figs. 13–14). $ALIVE_{GPP}$ is sensitive to frontal systems, diffuse radiation from wildfire aerosols, and $[O_3]$ concentrations on time scales of minutes to hours, but the specific responses to each are difficult to disentangle in the current iteration of our algorithm (Figs. S3 & S4). With ongoing improvements to data integration, cloud computing, and artificial intelligence, as well as forthcoming innovations in remote sensing including geostationary remote sensing, new carbon cycle data products can continue to be created that provide up-to-the-minute estimates of the carbon that enters the terrestrial biosphere.

CRediT authorship contribution statement

Danielle Losos: Writing – review & editing, Writing – original draft, Visualization, Validation, Software, Methodology, Investigation, Formal analysis, Data curation, Conceptualization. **Sadegh Ranjbar:** Writing – review & editing, Writing – original draft, Visualization, Validation, Software, Methodology, Investigation, Formal analysis, Data curation, Conceptualization. **Sophie Hoffman:** Writing – review & editing, Writing – original draft, Visualization, Validation, Software, Methodology, Investigation, Formal analysis, Data curation, Conceptualization. **Ryan Abernathey:** Writing – review & editing, Software, Resources, Methodology, Data curation. **Ankur R. Desai:** Writing – review & editing, Supervision, Resources, Project administration, Funding acquisition, Conceptualization. **Jason Otkin:** Writing – review & editing, Funding acquisition, Conceptualization. **Helin Zhang:** Writing – review & editing, Software, Resources, Data curation. **Youngryel Ryu:** Writing – review & editing, Supervision, Resources, Methodology, Data curation. **Paul C. Stoy:** Writing – review & editing, Writing – original draft, Visualization, Supervision, Resources, Project administration, Methodology, Investigation, Funding acquisition, Formal analysis, Data curation, Conceptualization.

Declaration of competing interest

Abernathy is Chief Executive Officer of Earthmover, whose Arraylake platform is employed in the present manuscript. Other authors declare that they have no known competing financial interests or personal relationships that could have appeared to influence the work reported in this paper.

Acknowledgements

We thank eddy covariance tower principal investigators and research teams for collecting eddy covariance data and the Ameriflux and NEON, Inc. network for organizing eddy covariance data and providing quality checks, hosting, and maintaining the eddy covariance databases. We likewise thank the GOES-R data providers. We thank Drs. Sam Batzli, Min Chen, Mutlu Özdoğan, Tim Schmit, and Zhou Zhang for critical insights. Support for this research was provided by the University of Wisconsin - Madison Office of the Vice Chancellor for Research and Graduate Education with funding from the Wisconsin Alumni Research Foundation. We also acknowledge support from the U.S. National Science Foundation Macrosystems Biology award 2106012 and Hydrological Sciences award 2422397, and the USDA Hatch program.

Appendix A. Supplementary data

Supplementary data to this article can be found online at https://doi.org/10.1016/j.rse.2025.114759.

Data availability

All data and code are fully and publicly available.

References

Abernathey, R.P., Augspurger, T., Banihirwe, A., Blackmon-Luca, C.C., Crone, T.J., Gentemann, C.L., Hamman, J.J., Henderson, N., Lepore, C., McCaie, T.A., 2021. Cloud-native repositories for big scientific data. Comput. Sci. Eng. 23, 26–35.

Alexander, C., Carley, J., Pyle, M., 2023. The *r*apid *r*efresh *f*orecast *s*ystem: *l*ooking beyond the first operational version. In: Presented at the 28th Conf. *O*n *N*umerical *W*eather *P*rediction.

Anderson, M.C., Norman, J.M., Meyers, T.P., Diak, G.R., 2000. An analytical model for estimating canopy transpiration and carbon assimilation fluxes based on canopy light-use efficiency. Agric. For. Meteorol. 101, 265–289.

Anderson, M.C., Norman, J.M., Mecikalski, J.R., Otkin, J.A., Kustas, W.P., 2007. A climatological study of evapotranspiration and moisture stress across the continental United States based on thermal remote sensing: 1. Model formulation. J. Geophys. Res. Atmos. 112 (D10). https://doi.org/10.1029/2006JD007506.

Anderson, M.C., Kustas, W.P., Norman, J.M., Hain, C.R., Mecikalski, J.R., Schultz, L., González-Dugo, M., Cammalleri, C., d'Urso, G., Pimstein, A., 2011. Mapping daily evapotranspiration at field to continental scales using geostationary and polar orbiting satellite imagery. Hydrol. Earth Syst. Sci. 15, 223–239.

Arkov, V., 2023. Uncertainty estimation in machine learning. In: 2023 International Russian Smart Industry Conference (SmartIndustryCon). Presented at the 2023 International Russian Smart Industry Conference (SmartIndustryCon), IEEE, Sochi. Russian Federation, pp. 130–135. https://doi.org/10.1109/SmartIndustryCon57312.2023.10110722.

Badgley, G., Field, C.B., Berry, J.A., 2017. Canopy near-infrared reflectance and terrestrial photosynthesis. Sci. Adv. 3, e1602244. https://doi.org/10.1126/sciadv.1602244.

Badgley, G., Anderegg, L.D.L., Berry, J.A., Field, C.B., 2019. Terrestrial gross primary production: using NIR $_V$ to scale from site to globe. Glob. Chang. Biol. 25, 3731–3740. https://doi.org/10.1111/gcb.14729.

Baldocchi, D., 2014. Measuring fluxes of trace gases and energy between ecosystems and the atmosphere–the state and future of the eddy covariance method. Glob. Chang. Biol. 20, 3600–3609.

Bucci, L., Alaka, L., Hagen, A., Delgado, S., Beven, J., 2023. National hurricane center tropical cyclone report. Hurric. Ian AL092022, 1–72.

Christian, J.I., Basara, J.B., Otkin, J.A., Hunt, E.D., Wakefield, R.A., Flanagan, P.X., Xiao, X., 2019. A methodology for flash drought identification: application of flash drought frequency across the United States. J. Hydrometeorol. 20, 833–846.

Christian, J.I., Basara, J.B., Hunt, E.D., Otkin, J.A., Furtado, J.C., Mishra, V., Xiao, X., Randall, R.M., 2021. Global distribution, trends, and drivers of flash drought occurrence. Nat. Commun. 12, 6330.

Christian, J.I., Martin, E.R., Basara, J.B., Furtado, J.C., Otkin, J.A., Lowman, L.E., Hunt, E.D., Mishra, V., Xiao, X., 2023. Global projections of flash drought show increased risk in a warming climate. Commun. Earth Environ. 4, 165.

Chu, H., Luo, X., Ouyang, Z., Chan, W.S., Dengel, S., Biraud, S.C., Torn, M.S., Metzger, S., Kumar, J., Arain, M.A., 2021. Representativeness of Eddy-covariance flux footprints for areas surrounding AmeriFlux sites. Agric. For. Meteorol. 301, 108350.

Coch, N.K., 2020. Inland damage from hurricanes. J. Coast. Res. 36, 1093–1105.

Corak, N.K., Otkin, J.A., Ford, T.W., Lowman, L.E., 2024. Unraveling phenological and stomatal responses to flash drought and implications for water and carbon budgets. Hydrol. Earth Syst. Sci. 28, 1827–1851.

Cuntz, M., 2020. *H*esseflux: A Python Library to Process and Post-Process Eddy Covariance Data. *https://zenodo.org/records/6954772*.

Dechant, B., Ryu, Y., Badgley, G., Köhler, P., Rascher, U., Migliavacca, M., Zhang, Y., Tagliabue, G., Guan, K., Rossini, M., 2022. NIR$_V$P: *a* robust structural proxy for sun-induced chlorophyll fluorescence and photosynthesis across scales. Remote Sens. Environ. 268, 112763.

DeFlorio, M.J., Sengupta, A., Castellano, C.M., Wang, J., Zhang, Z., Gershunov, A., Guirguis, K., Luna Niño, R., Clemesha, R.E., Pan, M., 2024. From California's extreme drought to major flooding: *e*valuating and synthesizing experimental seasonal and subseasonal forecasts of landfalling atmospheric rivers and extreme precipitation during *w*inter 2022/23. Bull. Am. Meteorol. Soc. 105, E84–E104.

Desai, A.R., Khan, A.M., Zheng, T., Paleri, S., Butterworth, B., Lee, T.R., Fisher, J.B., Hulley, G., Kleynhans, T., Gerace, A., 2021. Multi-sensor approach for high space and time resolution land surface temperature. Earth Space Sci. 8, e2021EA001842.

Diffenbaugh, N.S., Singh, D., Mankin, J.S., Horton, D.E., Swain, D.L., Touma, D., Charland, A., Liu, Y., Haugen, M., Tsiang, M., 2017. Quantifying the influence of global warming on unprecedented extreme climate events. Proc. Natl. Acad. Sci. 114, 4881–4886.

Dilling, L., 2007. Towards science in support of decision making: characterizing the supply of carbon cycle science. Environ. Sci. Pol. 10, 48–61.

Dowell, D.C., Alexander, C.R., James, E.P., Weygandt, S.S., Benjamin, S.G., Manikin, G. S., Blake, B.T., Brown, J.M., Olson, J.B., Hu, M., 2022. The *h*igh-*r*esolution *r*apid *r*efresh (HRRR): *a*n hourly updating convection-allowing forecast model. Part I: *m*otivation and system description. Weather Forecast. 37, 1371–1395.

Ferreira, R.R., Mutti, P., Mendes, K.R., Campos, S., Marques, T.V.P., Oliveira, C., Gonçalves, W., Mota, J., Difante, G., Urbano, S.A., 2021. An assessment of the MOD17A2 gross primary production product in the Caatinga biome, Brazil. Int. J. Remote Sens. 42, 1275–1291.

Fu, Z., Gerken, T., Bromley, G., Araújo, A., Bonal, D., Burban, B., Ficklin, D., Fuentes, J. D., Goulden, M., Hirano, T., 2018. The surface-atmosphere exchange of carbon dioxide in tropical rainforests: *s*ensitivity to environmental drivers and flux measurement methodology. Agric. For. Meteorol. 263, 292–307.

Fu, Z., Ciais, P., Prentice, I.C., Gentine, P., Makowski, D., Bastos, A., Luo, X., Green, J.K., Stoy, P.C., Yang, H., 2022. Atmospheric dryness reduces photosynthesis along a large range of soil water deficits. Nat. Commun. 13, 989.

Fu, D., Gueymard, C.A., Xia, X., 2023. Validation of the improved GOES-16 aerosol optical depth product over North America. Atmos. Environ. 298, 119642.

Ghassemian, H., 2016. A review of remote sensing image fusion methods. Inf. Fusion 32, 75–89.

Grace, J., 2004. Understanding and managing the global carbon cycle. J. Ecol. 92, 189–202.

Grassi, G., Vicinelli, E., Ponti, F., Cantoni, L., Magnani, F., 2005. Seasonal and interannual variability of photosynthetic capacity in relation to leaf nitrogen in a deciduous forest plantation in northern Italy. Tree Physiol. 25, 349–360.

Grim, J.A., Pinto, J.O., Dowell, D.C., 2024. Assessing RRFS versus HRRR in *p*redicting *w*idespread convective *s*ystems over the *e*astern CONUS. Weather Forecast. 39, 121–140.

Gu, L., Shuai, Y., Shao, C., Xie, D., Zhang, Q., Li, Y., Yang, J., 2021. Angle effect on typical optical remote sensing indices in vegetation monitoring. Remote Sens. 13, 1699.

Hartley, A., MacBean, N., Georgievski, G., Bontemps, S., 2017. Uncertainty in plant functional type distributions and its impact on land surface models. Remote Sens. Environ. 203, 71–89.

He, T., Zhang, Y., Liang, S., Yu, Y., Wang, D., 2019. Developing land surface directional reflectance and albedo products from geostationary GOES-R and Himawari data: *t*heoretical basis, operational implementation, and validation. Remote Sens. 11, 2655.

Heidinger, A.K., Pavolonis, M.J., Calvert, C., Hoffman, J., Nebuda, S., Straka III, W., Walther, A., Wanzong, S., 2020. ABI cloud products from the GOES-R series. In: The GOES-R Series. Elsevier, pp. 43–62.

Heinsch, F.A., Zhao, M., Running, S.W., Kimball, J.S., Nemani, R.R., Davis, K.J., Bolstad, P.V., Cook, B.D., Desai, A.R., Ricciuto, D.M., 2006. Evaluation of remote sensing based terrestrial productivity from MODIS using regional tower eddy flux network observations. IEEE Trans. Geosci. Remote Sens. 44, 1908–1925.

James, E.P., Alexander, C.R., Dowell, D.C., Weygandt, S.S., Benjamin, S.G., Manikin, G. S., Brown, J.M., Olson, J.B., Hu, M., Smirnova, T.G., 2022. The *h*igh-*r*esolution *r*apid *r*efresh (HRRR): *a*n hourly updating convection-allowing forecast model. Part II: Forecast Perform. Weather Forecast. 37, 1397–1417.

Jeong, S., Ryu, Y., Dechant, B., Li, X., Kong, J., Choi, W., Kang, M., Yeom, J., Lim, J., Jang, K., 2023. Tracking diurnal to seasonal variations of gross primary productivity using a geostationary satellite, GK-2A advanced meteorological imager. Remote Sens. Environ. 284, 113365.

Jeong, S., Ryu, Y., Li, X., Dechant, B., Liu, J., Kong, J., Choi, W., Fang, J., Lian, X., Gentine, P., 2024. GEOSIF: a *c*ontinental-*s*cale *s*ub-*d*aily *r*econstructed *s*olar-*i*nduced *f*luorescence *d*erived from OCO-3 and GK-2A over Eastern Asia and Oceania. Remote Sens. Environ. 311, 114284.

Jiang, C., Guan, K., Wu, G., Peng, B., Wang, S., 2021. A daily, 250 m and real-time gross primary productivity product (2000–present) covering the contiguous United States. Earth Syst. Sci. Data 13, 281–298.

Jung, M., Reichstein, M., Bondeau, A., 2009. Towards global empirical upscaling of FLUXNET eddy covariance observations: validation of a model tree ensemble approach using a biosphere model. Biogeosciences 6, 2001–2013.

Jung, M., Schwalm, C., Migliavacca, M., Walther, S., Camps-Valls, G., Koirala, S., Anthoni, P., Besnard, S., Bodesheim, P., Carvalhais, N., 2020. Scaling carbon fluxes from eddy covariance sites to globe: synthesis and evaluation of the FLUXCOM approach. Biogeosciences 17, 1343–1365.

Kebede, H., Fisher, D.K., Sui, R., Reddy, K.N., 2014. Irrigation methods and scheduling in the Delta region of Mississippi: current status and strategies to improve irrigation efficiency. Am. J. Plant Sci. 5, 2917.

Khan, A.M., Stoy, P.C., Douglas, J.T., Anderson, M., Diak, G., Otkin, J.A., Hain, C., Rehbein, E.M., McCorkel, J., 2021. Reviews and syntheses: *o*ngoing and emerging opportunities to improve environmental science using observations from the *a*dvanced *b*aseline *i*mager on the *g*eostationary *o*perational *e*nvironmental *s*atellites. Biogeosciences 18, 4117–4141.

Khan, A.M., Stoy, P., Joiner, J., Baldocchi, D., Verfaillie, J., Chen, M., Otkin, J., 2022. The diurnal dynamics of gross primary productivity using observations from the *a*dvanced *b*aseline *i*mager on the *g*eostationary *o*perational *e*nvironmental *s*atellite-R *s*eries at an oak savanna ecosystem. J. Geophys. Res. Biogeosci. 127, e2021JG006701.

Kondragunta, S., Laszlo, I., Zhang, H., Ciren, P., Huff, A., 2020. Air quality applications of ABI aerosol products from the GOES-R series. GOES-R Ser. 203–217.

Lasslop, G., Reichstein, M., Papale, D., Richardson, A.D., Arneth, A., Barr, A., Stoy, P., Wohlfahrt, G., 2010. Separation of net ecosystem exchange into assimilation and respiration using a light response curve approach: critical issues and global evaluation. Glob. Chang. Biol. 16, 187–208.

Laszlo, I., Liu, H., Kim, H.-Y., Pinker, R.T., 2020. Shortwave radiation from ABI on the GOES-R *s*eries. In: The GOES-R Series. Elsevier, pp. 179–191.

Leeper, R.D., Bilotta, R., Petersen, B., Stiles, C.J., Heim, R., Fuchs, B., Prat, O.P., Palecki, M., Ansari, S., 2022. Characterizing US drought over the past 20 years using the US drought monitor. Int. J. Climatol. 42, 6616–6630.

Li, Y., Wu, H., Li, Z.-L., Duan, S., Ni, L., 2020. Evaluation of spatiotemporal fusion models in land surface temperature using polar-orbiting and geostationary satellite data. In: Presented at the IGARSS 2020–2020 IEEE International Geoscience and Remote Sensing Symposium. IEEE, pp. 236–239.

Li, B., Ryu, Y., Jiang, C., Dechant, B., Liu, J., Yan, Y., Li, X., 2023a. BESSv2. 0: *a* satellite-based and coupled-process model for quantifying long-term global land–atmosphere fluxes. Remote Sens. Environ. 295, 113696.

Li, X., Ryu, Y., Xiao, J., Dechant, B., Liu, J., Li, B., Jeong, S., Gentine, P., 2023b. New-generation geostationary satellite reveals widespread midday depression in dryland photosynthesis during 2020 western US heatwave. Sci. Adv. 9, eadi0775.

Li, R., Wang, D., Wang, W., Nemani, R., 2023c. A GeoNEX-based high-spatiotemporal-resolution product of land surface downward shortwave radiation and photosynthetically active radiation. Earth Syst. Sci. Data 15, 1419–1436.

Lindsey, D.T., Heidinger, A.K., Sullivan, P.C., McCorkel, J., Schmit, T.J., Tomlinson, M., Vandermeulen, R., Frost, G.J., Kondragunta, S., Rudlosky, S., 2024. GeoXO: NOAA*'S* *f*uture *g*eostationary *s*atellite *s*ystem. Bull. Am. Meteorol. 105, E660–E679.

Lobell, D., Asner, G., Law, B., Treuhaft, R., 2002. View angle effects on canopy reflectance and spectral mixture analysis of coniferous forests using AVIRIS. Int. J. Remote Sens. 23, 2247–2262.

Losos, D., Hoffman, S., Stoy, P.C., 2024. GOES-R land surface products at Western *h*emisphere eddy covariance tower locations. Sci. Data 11, 277.

Lowman, L.E., Barros, A.P., 2016. Interplay of drought and tropical cyclone activity in SE US gross primary productivity. J. Geophys. Res. Biogeosci. 121, 1540–1567.

Lumumba, V.W., Kiprotich, D., Makena, N.G., Kavita, M.D., 2024. Comparative analysis of cross-validation techniques: LOOCV, k-folds cross-validation, and repeated k-folds cross-validation in machine learning models. Am. J. Theor. Appl. Stat. 13, 127–137.

McCorkel, J., Van Naarden, J., Lindsey, D., Efremova, B., Coakley, M., Black, M., Krimchansky, A., 2019. GOES-17 advanced baseline imager performance recovery summary. In: Presented at the IGARSS 2019–2019 IEEE International Geoscience and Remote Sensing Symposium. IEEE, pp. 1–4.
Menzel, W.P., 2020. History of geostationary weather satellites. In: The GOES-R Series. Elsevier, pp. 5–11.
Miura, T., Nagai, S., Takeuchi, M., Ichii, K., Yoshioka, H., 2019. Improved characterisation of vegetation and land surface seasonal dynamics in central Japan with Himawari-8 hypertemporal data. Scientific Reports 30, 15692.
Naeger, A.R., Newchurch, M.J., Moore, T., Chance, K., Liu, X., Alexander, S., Murphy, K., Wang, B., 2021. Revolutionary air-pollution applications from future tropospheric emissions: monitoring of pollution (TEMPO) observations. Bull. Am. Meteorol. Soc. 102, E1735–E1741.
Nelson, J.A., Walther, S., Kraft, B., Gans, F., Duveiller, G., Weber, U., Hamdi, Z.M., Zhang, W., Jung, M., 2024. Terrestrial carbon and water flux products from an extended data-driven scaling framework. In: FLUXCOM-X. Copernicus Meetings.
Nemani, R., Wang, W., Hashimoto, H., Michaelis, A., Vandal, T., Lyapustin, A., Zhang, J., Lee, T., Kalluri, S., Takenaka, H., 2020. GeoNEX: A geostationary earth observatory at NASA Earth Exchange: earth monitoring from operational geostationary satellite systems. In: Presented at the IGARSS 2020–2020 IEEE International Geoscience and Remote Sensing Symposium. IEEE, pp. 128–131.
Novick, K.A., Ficklin, D.L., Stoy, P.C., Williams, C.A., Bohrer, G., Oishi, A.C., Papuga, S. A., Blanken, P.D., Noormets, A., Sulman, B.N., 2016. The increasing importance of atmospheric demand for ecosystem water and carbon fluxes. Nat. Clim. Chang. 6, 1023–1027.
Otkin, J.A., Anderson, M.C., Hain, C., Mladenova, I.E., Basara, J.B., Svoboda, M., 2013. Examining rapid onset drought development using the thermal infrared–based evaporative stress index. J. Hydrometeorol. 14, 1057–1074.
Otkin, J.A., Svoboda, M., Hunt, E.D., Ford, T.W., Anderson, M.C., Hain, C., Basara, J.B., 2018. Flash droughts: a review and assessment of the challenges imposed by rapid-onset droughts in the United States. Bull. Am. Meteorol. Soc. 99, 911–919.
Pabon-Moreno, D.E., Migliavacca, M., Reichstein, M., Mahecha, M.D., 2022. On the potential of Sentinel-2 for estimating gross primary production. IEEE Trans. Geosci. Remote Sens. 60, 1–12.
Papale, D., Valentini, R., 2003. A new assessment of European forests carbon exchanges by eddy fluxes and artificial neural network spatialization. Glob. Chang. Biol. 9, 525–535.
Papale, D., Reichstein, M., Aubinet, M., Canfora, E., Bernhofer, C., Kutsch, W., Longdoz, B., Rambal, S., Valentini, R., Vesala, T., 2006. Towards a standardized processing of net ecosystem exchange measured with eddy covariance technique: algorithms and uncertainty estimation. Biogeosciences 3, 571–583.
Parazoo, N., Osman, M., Pascolini-Campbell, M., Byrne, B., 2024. Antecedent conditions mitigate carbon loss during flash drought events. Geophys. Res. Lett. 51, e2024GL108310.
Parente, L., Taquary, E., Silva, A.P., Souza Jr., C., Ferreira, L., 2019. Next generation mapping: combining deep learning, cloud computing, and big remote sensing data. Remote Sens. 11, 2881.
Pastorello, G., Trotta, C., Canfora, E., Chu, H., Christianson, D., Cheah, Y.-W., Poindexter, C., Chen, J., Elbashandy, A., Humphrey, M., 2020. The FLUXNET2015 dataset and the ONEFlux processing pipeline for eddy covariance data. Sci. Data 7, 1–27.
Pavlick, R., Drewry, D.T., Bohn, K., Reu, B., Kleidon, A., 2013. The Jena diversity-dynamic global vegetation model (JeDi-DGVM): a diverse approach to representing terrestrial biogeography and biogeochemistry based on plant functional trade-offs. Biogeosciences 10, 4137–4177.
Pedregosa, F., Varoquaux, G., Gramfort, A., Michel, V., Thirion, B., Grisel, O., Blondel, M., Prettenhofer, P., Weiss, R., Dubourg, V., 2011. Scikit-learn: machine learning in Python. J. Mach. Learn. Res. 12, 2825–2830.
Prentice, I.C., Balzarolo, M., Bloomfield, K.J., Chen, J.M., Dechant, B., Ghent, D., Janssens, I.A., Luo, X., Morfopoulos, C., Ryu, Y., 2024. Principles for satellite monitoring of vegetation carbon uptake. Nat. Rev. Earth Environ. 1–15.
Ranjbar, S., Losos, D., Dechant, B., Hoffman, S., Başakın, E.E., Stoy, P.C., 2024a. Harnessing information from shortwave infrared reflectance bands to enhance satellite-based estimates of gross primary productivity. J. Geophys. Res. Biogeosciences 129 (11), e2024JG008240. https://doi.org/10.1029/2024JG008240.
Ranjbar, S., Losos, D., Hoffman, S., Arabi, S., Desai, A.R., Stoy, P.C., 2024b. Near real-time mapping of all-sky land surface temperature from GOES-R using machine learning. ESS Open Arch. https://doi.org/10.22541/essoar.172801403.30077549/v1.
Ranjbar, S., Losos, D., Hoffman, S., Cuntz, M., Stoy, P.C., 2024c. Using geostationary satellite observations and machine learning models to estimate ecosystem carbon uptake and respiration at half hourly time steps at eddy covariance sites. J. Adv. Model. Earth Syst. 16, e2024MS004341.
Ranjbar, S., Losos, D., Hoffman, S., Stoy, P.C., 2024d. High-frequency mapping of downward shortwave radiation from GOES-R using gradient boosting. IEEE J. Sel. Top. Appl. Earth Obs. Remote Sens. 17, 11958–11968. https://doi.org/10.1109/JSTARS.2024.3420148.
Reichstein, M., Falge, E., Baldocchi, D., Papale, D., Aubinet, M., Berbigier, P., Bernhofer, C., Buchmann, N., Gilmanov, T., Granier, A., 2005. On the separation of net ecosystem exchange into assimilation and ecosystem respiration: review and improved algorithm. Glob. Chang. Biol. 11, 1424–1439.
Reichstein, M., Stoy, P.C., Desai, A.R., Lasslop, G., Richardson, A.D., 2012. Partitioning of net fluxes. Eddy Covariance Pract. Guide Meas. Data Anal. 263–289.
Reed, D., Chavez, S., Castañeda-Moya, E., Oberbauer, S.F., Troxler, T., Malone, S., 2025. Resilience to hurricanes is high in mangrove blue carbon forests. Glob. Change Biol. 31, e70124.
Reichstein, M., Bahn, M., Ciais, P., Frank, D., Mahecha, M.D., Seneviratne, S.I., Zscheischler, J., Beer, C., Buchmann, N., Frank, D.C., 2013. Climate extremes and the carbon cycle. Nature 500, 287–295.
Richardson, A.D., Hollinger, D.Y., Burba, G.G., Davis, K.J., Flanagan, L.B., Katul, G.G., Munger, J.W., Ricciuto, D.M., Stoy, P.C., Suyker, A.E., 2006. A multi-site analysis of random error in tower-based measurements of carbon and energy fluxes. Agric. For. Meteorol. 136, 1–18.
Richardson, A.D., Hufkens, K., Milliman, T., Aubrecht, D.M., Chen, M., Gray, J.M., Johnston, M.R., Keenan, T.F., Klosterman, S.T., Kosmala, M., 2018. Tracking vegetation phenology across diverse north American biomes using PhenoCam imagery. Sci. Data 5, 1–24.
Runkle, B.R., Rigby, J.R., Reba, M.L., Anapalli, S.S., Bhattacharjee, J., Krauss, K.W., Liang, L., Locke, M.A., Novick, K.A., Sui, R., 2017. Delta-flux: an eddy covariance network for a climate-smart lower Mississippi Basin. Agric. Environ. Lett. 2, ael2017-01.
Running, S.W., Zhao, M., 2015. Daily GPP and annual NPP (MOD17A2/A3) products NASA earth observing system MODIS land algorithm. In: MOD17 User's Guide 2015, pp. 1–28.
Running, S.W., Nemani, R.R., Heinsch, F.A., Zhao, M., Reeves, M., Hashimoto, H., 2004. A continuous satellite-derived measure of global terrestrial primary production. Bioscience 54, 547–560.
Ryu, Y., 2024. Upscaling land surface fluxes through hyper resolution remote sensing in space, time, and the spectrum. J. Geophysical Res. Biogeosci. 129, e2023JG007678.
Schimel, D., Pavlick, R., Fisher, J.B., Asner, G.P., Saatchi, S., Townsend, P., Miller, C., Frankenberg, C., Hibbard, K., Cox, P., 2015. Observing terrestrial ecosystems and the carbon cycle from space. Glob. Chang. Biol. 21, 1762–1776.
Schmidt, C., 2020. Monitoring fires with the GOES-R series. In: The GOES-R Series. Elsevier, pp. 145–163.
Schmit, T.J., Gunshor, M.M., 2020. ABI imagery from the GOES-R series. In: The GOES-R Series. Elsevier, pp. 23–34.
Schmit, T.J., Griffith, P., Gunshor, M.M., Daniels, J.M., Goodman, S.J., Lebair, W.J., 2017. A closer look at the ABI on the GOES-R series. Bull. Am. Meteorol. Soc. 98, 681–698.
Schmit, T.J., Li, Z., Gunshor, M.M., Iturbide-Iturbide, F., Yoe, J.G., McCorkel, J., Heidinger, A., 2022. US Plans for geostationary hyperspectral infrared sounders. In: Presented at the IGARSS 2022–2022 IEEE International Geoscience and Remote Sensing Symposium, IEEE, pp. 5411–5414.
Seyednasrollah, B., Young, A.M., Hufkens, K., Milliman, T., Friedl, M.A., Frolking, S., Richardson, A.D., 2019. Tracking vegetation phenology across diverse biomes using version 2.0 of the PhenoCam dataset. Sci. Data 6, 222.
Shapley, L.S., 1951. Notes on the N-Person Game—II: The Value of an N-Person Game.
Silveira, M., 2021. AmeriFlux FLUXNET-1F US-ONA Florida Pine Flatwoods. Lawrence Berkeley National Lab (LBNL), Berkeley, CA.
Simone, G., Farina, A., Morabito, F.C., Serpico, S.B., Bruzzone, L., 2002. Image fusion techniques for remote sensing applications. Inf. Fusion 3, 3–15.
Sippel, S., Reichstein, M., Ma, X., Mahecha, M.D., Lange, H., Flach, M., Frank, D., 2018. Drought, heat, and the carbon cycle: a review. Curr. Clim. Chang. Rep. 4, 266–286.
Sjöström, M., Zhao, M., Archibald, S., Arneth, A., Cappelaere, B., Falk, U., De Grandcourt, A., Hanan, N., Kergoat, L., Kutsch, W., 2013. Evaluation of MODIS gross primary productivity for Africa using eddy covariance data. Remote Sens. Environ. 131, 275–286.
Sluijterman, L., Cator, E., Heskes, T., 2024. How to evaluate uncertainty estimates in machine learning for regression? Neural Netw. 173, 106203. https://doi.org/10.1016/j.neunet.2024.106203.
Stocker, B.D., Zscheischler, J., Keenan, T.F., Prentice, I.C., Seneviratne, S.I., Peñuelas, J., 2019. Drought impacts on terrestrial primary production underestimated by satellite monitoring. Nat. Geosci. 12, 264–270.
Stoy, P.C., Katul, G.G., Siqueira, M.B., Juang, J.-Y., Novick, K.A., Uebelherr, J.M., Oren, R., 2006. An evaluation of models for partitioning eddy covariance-measured net ecosystem exchange into photosynthesis and respiration. Agric. For. Meteorol. 141, 2–18.
Stoy, P.C., Ahmed, S., Jarchow, M., Rashford, B., Swanson, D., Albeke, S., Bromley, G., Brookshire, E., Dixon, M.D., Haggerty, J., 2018. Opportunities and trade-offs among BECCS and the food, water, energy, biodiversity, and social systems nexus at regional scales. BioScience 68, 100–111.
Sun, J., Zhang, Y., Wu, Z., Zhu, Y., Yin, X., Ding, Z., Wei, Z., Plaza, J., Plaza, A., 2019. An efficient and scalable framework for processing remotely sensed big data in cloud computing environments. IEEE Trans. Geosci. Remote Sens. 57, 4294–4308.
Suomi, V.E., Parent, R.J., 1968. A color view of planet earth. Bull. Am. Meteorol. Soc. 49, 74–75.
Svoboda, M., LeComte, D., Hayes, M., Heim, R., Gleason, K., Angel, J., Rippey, B., Tinker, R., Palecki, M., Stooksbury, D., 2002. The drought monitor. Bull. Am. Meteorol. Soc. 83, 1181–1190.
Tramontana, G., Ichii, K., Camps-Valls, G., Tomelleri, E., Papale, D., 2015. Uncertainty analysis of gross primary production upscaling using random forests, remote sensing and eddy covariance data. Remote Sens. Environ. 168, 360–373.
Tumber-Dávila, S.J., Lucey, T., Boose, E.R., Laflower, D., León-Sáenz, A., Wilson, B.T., MacLean, M.G., Thompson, J.R., 2024. Hurricanes pose a substantial risk to New England forest carbon stocks. Glob. Chang. Biol. 30, e17259.
Turner, D.P., Ritts, W.D., Cohen, W.B., Gower, S.T., Running, S.W., Zhao, M., Costa, M. H., Kirschbaum, A.A., Ham, J.M., Saleska, S.R., 2006. Evaluation of MODIS NPP and GPP products across multiple biomes. Remote Sens. Environ. 102, 282–292.

Turner, H.C., Galford, G.L., Hernandez Lopez, N., Falcón Méndez, A., Borroto-Escuela, D. Y., Hernández Ramos, I., González-Díaz, P., 2023. Extent, severity, and temporal patterns of damage to Cuba's ecosystems following *h*urricane Irma: MODIS and Sentinel-2 *h*urricane *d*isturbance *v*egetation *a*nomaly (HDVA). Remote Sens. 15, 2495.

Ukkola, A., De Kauwe, M., Pitman, A., Best, M., Abramowitz, G., Haverd, V., Decker, M., Haughton, N., 2016. Land surface models systematically overestimate the intensity, duration and magnitude of seasonal-scale evaporative droughts. Environ. Res. Lett. 11, 104012.

Wang, F., D'Sa, E.J., 2009. Potential of MODIS EVI in identifying hurricane disturbance to coastal vegetation in the northern Gulf of Mexico. Remote Sens. 2, 1–18.

Wang, D., Li, R., 2022. A GeoNEX-based 1km hourly land surface downward shortwave radiation (DSR) and photosynthetically active radiation (PAR) product. Zenodo [data set]. Zenodo Data Set 10.

Wang, C., Chen, J., Wu, J., Tang, Y., Shi, P., Black, T.A., Zhu, K., 2017. A snow-free vegetation index for improved monitoring of vegetation spring green-up date in deciduous ecosystems. Remote Sens. Environ. 196, 1–12.

Wang, W., Li, S., Hashimoto, H., Takenaka, H., Higuchi, A., Kalluri, S., Nemani, R., 2020. An introduction to the *g*eostationary-NASA *e*arth *e*xchange (GeoNEX) *p*roducts: 1. Top-of-atmosphere reflectance and brightness temperature. Remote Sens. 12, 1267.

Watine-Guiu, M., Varon, D.J., Irakulis-Loitxate, I., Balasus, N., Jacob, D.J., 2023. Geostationary satellite observations of extreme and transient methane emissions from oil and gas infrastructure. Proc. Natl. Acad. Sci. 120, e2310797120.

Way, D.A., Stinziano, J.R., Berghoff, H., Oren, R., 2017. How well do growing season dynamics of photosynthetic capacity correlate with leaf biochemistry and climate fluctuations? Tree Physiol. 37, 879–888.

Wheeler, K.I., Dietze, M.C., 2019. A statistical model for estimating midday NDVI from the geostationary operational environmental satellite (GOES) 16 and 17. Remote Sens. 11, 2507.

Wheeler, K.I., Dietze, M.C., 2021. Improving the monitoring of deciduous broadleaf phenology using the *g*eostationary *o*perational *e*nvironmental *s*atellite (GOES) 16 and 17. Biogeosciences 18, 1971–1985.

Wilson, K.B., Baldocchi, D.D., Hanson, P.J., 2000. Spatial and seasonal variability of photosynthetic parameters and their relationship to leaf nitrogen in a deciduous forest. Tree Physiol. 20, 565–578.

Wu, P., Shen, H., Zhang, L., Göttsche, F.-M., 2015. Integrated fusion of multi-scale polar-orbiting and geostationary satellite observations for the mapping of high spatial and temporal resolution land surface temperature. Remote Sens. Environ. 156, 169–181.

Wulder, M.A., Loveland, T.R., Roy, D.P., Crawford, C.J., Masek, J.G., Woodcock, C.E., Allen, R.G., Anderson, M.C., Belward, A.S., Cohen, W.B., 2019. Current status of Landsat program, science, and applications. Remote Sens. Environ. 225, 127–147.

Wutzler, T., Lucas-Moffat, A., Migliavacca, M., Knauer, J., Sickel, K., Šigut, L., Menzer, O., Reichstein, M., 2018. Basic and extensible post-processing of eddy covariance flux data with REddyProc. Biogeosciences 15, 5015–5030.

Xiao, J., Chevallier, F., Gomez, C., Guanter, L., Hicke, J.A., Huete, A.R., Ichii, K., Ni, W., Pang, Y., Rahman, A.F., 2019. Remote sensing of the terrestrial carbon cycle: *a* review of advances over 50 years. Remote Sens. Environ. 233, 111383.

Xiao, J., Fisher, J.B., Hashimoto, H., Ichii, K., Parazoo, N.C., 2021. Emerging satellite observations for diurnal cycling of ecosystem processes. Nat. Plants 7, 877–887.

Xu, D., Wang, C., Chen, Jin, Shen, M., Shen, B., Yan, R., Li, Z., Karnieli, A., Chen, Jiquan, Yan, Y., 2021. The superiority of the normalized difference phenology index (NDPI) for estimating grassland aboveground fresh biomass. Remote Sens. Environ. 264, 112578.

Yan, J., Ma, Y., Wang, L., Choo, K.-K.R., Jie, W., 2018. A cloud-based remote sensing data production system. Futur. Gener. Comput. Syst. 86, 1154–1166.

Yasarer, L.M., Taylor, J.M., Rigby, J.R., Locke, M.A., 2020. Trends in land use, irrigation, and streamflow alteration in the Mississippi River *a*lluvial *p*lain. Front. Environ. Sci. 8, 66.

Yoon, D., Chen, J.-H., Seo, E., 2024. Contribution of land-atmosphere coupling in 2022 CONUS compound drought-heatwave events and implications for forecasting. Weather Clim. Extrem. 46, 100722.

Yu, Y., Yu, P., 2020. Land surface temperature product from the GOES-R series. In: The GOES-R Series. Elsevier, pp. 133–144.

Yu, Y., Tarpley, D., Privette, J.L., Goldberg, M.D., Raja, M.R.V., Vinnikov, K.Y., Xu, H., 2008. Developing algorithm for operational GOES-R land surface temperature product. IEEE Trans. Geosci. Remote Sens. 47, 936–951.

Yuan, X., Wang, Y., Ji, P., Wu, P., Sheffield, J., Otkin, J.A., 2023. A global transition to flash droughts under climate change. Science 380, 187–191.

Zeng, Y., Hao, D., Huete, A., Dechant, B., Berry, J., Chen, J.M., Joiner, J., Frankenberg, C., Bond-Lamberty, B., Ryu, Y., 2022. Optical vegetation indices for monitoring terrestrial ecosystems globally. Nat. Rev. Earth Environ. 3, 477–493.

Zhang, M., Yuan, X., 2020. Rapid reduction in ecosystem productivity caused by flash droughts based on decade-long FLUXNET observations. Hydrol. Earth Syst. Sci. 24, 5579–5593.

Zhang, H., Kondragunta, S., Laszlo, I., Zhou, M., 2020. Improving GOES *a*dvanced *b*aseline *i*mager (ABI) aerosol optical depth (AOD) retrievals using an empirical bias correction algorithm. Atmos. Meas. Tech. 13, 5955–5975.

Zoogman, P., Liu, X., Suleiman, R., Pennington, W., Flittner, D., Al-Saadi, J., Hilton, B., Nicks, D., Newchurch, M., Carr, J., 2017. Tropospheric emissions: *m*onitoring of pollution (TEMPO). J. Quant. Spectrosc. Radiat. Transf. 186, 17–39.

Zscheischler, J., Mahecha, M.D., Von Buttlar, J., Harmeling, S., Jung, M., Rammig, A., Randerson, J.T., Schölkopf, B., Seneviratne, S.I., Tomelleri, E., 2014. A few extreme events dominate global interannual variability in gross primary production. Environ. Res. Lett. 9, 035001.